AGU PUBLICATIONS

JGR

Journal of Geophysical Research: Planets

RESEARCH ARTICLE

10.1002/2014JE004715

Key Points:
- The Mars Global Ionosphere-Thermosphere Model (MGITM) is presented and validated
- MGITM captures solar cycle, seasonal, and diurnal trends observed above 100 km
- MGITM variations will be compared to key episodic variations in future studies

Correspondence to:
S. W. Bougher,
bougher@umich.edu

Citation:
Bougher, S. W., D. Pawlowski, J. M. Bell, S. Nelli, T. McDunn, J. R. Murphy, M. Chizek, and A. Ridley (2015), Mars Global Ionosphere-Thermosphere Model (MGITM): Solar cycle, seasonal, and diurnal variations of the Mars upper atmosphere, *J. Geophys. Res. Planets*, *120*, 311–342, doi:10.1002/2014JE004715.

Received 13 AUG 2014
Accepted 23 DEC 2014
Accepted article online 29 DEC 2014
Published online 26 FEB 2015

Mars Global Ionosphere-Thermosphere Model: Solar cycle, seasonal, and diurnal variations of the Mars upper atmosphere

S. W. Bougher[1], D. Pawlowski[2], J. M. Bell[3], S. Nelli[4], T. McDunn[5], J. R. Murphy[6], M. Chizek[6], and A. Ridley[1]

[1] Atmospheric, Oceanic, and Space Sciences Department, University of Michigan, Ann Arbor, Michigan, USA, [2] Physics Department, Eastern Michigan University, Ypsilanti, Michigan, USA, [3] National Institute of Aerospace, Hampton, Virginia, USA, [4] Harris, ITS, Las Cruces, New Mexico, USA, [5] Jet Propulsion Laboratory, Pasadena, California, USA, [6] Astronomy Department, New Mexico State University, Las Cruces, New Mexico, USA

Abstract A new Mars Global Ionosphere-Thermosphere Model (M-GITM) is presented that combines the terrestrial GITM framework with Mars fundamental physical parameters, ion-neutral chemistry, and key radiative processes in order to capture the basic observed features of the thermal, compositional, and dynamical structure of the Mars atmosphere from the ground to the exosphere (0–250 km). Lower, middle, and upper atmosphere processes are included, based in part upon formulations used in previous lower and upper atmosphere Mars GCMs. This enables the M-GITM code to be run for various seasonal, solar cycle, and dust conditions. M-GITM validation studies have focused upon simulations for a range of solar and seasonal conditions. Key upper atmosphere measurements are selected for comparison to corresponding M-GITM neutral temperatures and neutral-ion densities. In addition, simulated lower atmosphere temperatures are compared with observations in order to provide a first-order confirmation of a realistic lower atmosphere. M-GITM captures solar cycle and seasonal trends in the upper atmosphere that are consistent with observations, yielding significant periodic changes in the temperature structure, the species density distributions, and the large-scale global wind system. For instance, mid afternoon temperatures near ~200 km are predicted to vary from ~210 to 350 K (equinox) and ~190 to 390 k (aphelion to perihelion) over the solar cycle. These simulations will serve as a benchmark against which to compare episodic variations (e.g., due to solar flares and dust storms) in future M-GITM studies. Additionally, M-GITM will be used to support MAVEN mission activities (2014–2016).

1. Introduction and Motivation

The detailed characterization of the structure and dynamics of the Mars lower (0–50 km), middle (~50–100 km), and upper (~100–250 km) atmospheres is important for conducting future Mars aerobraking, aerocapture, descent, and landing activities and also to understand the fundamental processes that maintain and drive variations in the present Mars atmosphere and climate system [*MEPAG Goals Committee*, 2010]. Strong coupling processes linking the Mars lower to upper atmospheres are crucial to quantify in order to predict upper atmosphere densities, temperatures, winds, and waves in preparation for these spacecraft operations. It is recognized that the entire Mars atmosphere is an integrated system that must be treated as a whole from the ground to the exobase. Numerical modeling efforts must be tailored to address this integrated Mars system in order to reliably simulate the state and variations of the Mars lower, middle, and upper atmospheres over various timescales (e.g., solar cycle, seasonal, and diurnal). In this paper, we specifically focus upon the upper atmosphere responses to external forcing processes, and the resulting solar cycle, seasonal, and diurnal variations.

1.1. Coupling of Thermosphere-Ionosphere to Regions Above and Below

The Mars thermosphere (~100–200 km) is an intermediate atmospheric region strongly impacted by coupling from below with the lower-middle atmosphere (via gravity waves, planetary waves and tides, and dust storms) and coupling from above with the exosphere and ultimately the Sun (via solar radiation and solar wind particles, see Figure 1) [e.g., *Bougher et al.*, 2002, 2008, 2014a]. The thermospheric layer extends from the top of the middle atmosphere (defined as the mesopause) to the beginning of space (exobase). Thermospheric temperatures typically increase from the mesopause to the exobase, with underlying neutral

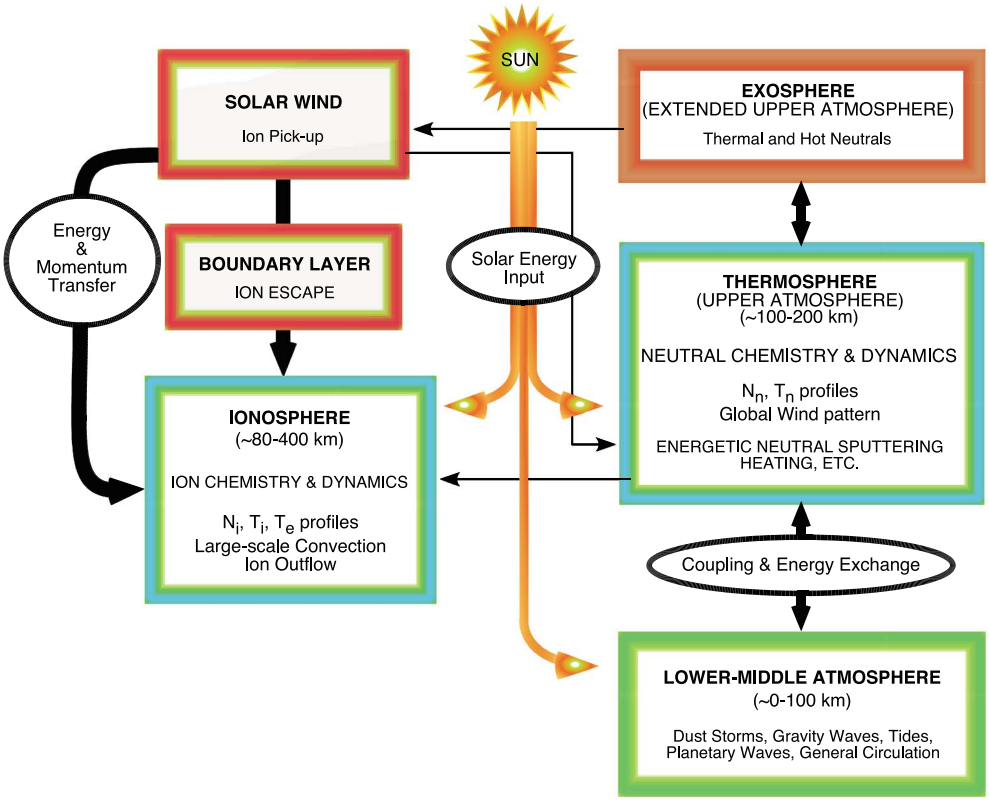

Figure 1. Cartoon of Mars atmospheric regions and processes. Illustrates the coupling of the thermosphere and ionosphere with atmospheric regions above and below. Taken from *Bougher et al.* [2014b], Figure 1, Space Science Reviews. Reproduced with kind permission from Springer Science and Business Media.

densities dominated by CO_2 that give way to atomic O near 200 km. Embedded largely within the thermosphere and exosphere is the ionosphere (~80–400 km), a weakly ionized plasma. The primary charged particles that make up the Mars ionosphere (e.g., O_2^+, CO_2^+, O^+, CO^+, and NO^+) are formed by the following: (1) solar EUV fluxes and subsequent photoelectrons that ionize local neutral thermospheric species (e.g., CO_2, O, N_2, and CO), (2) precipitating particles (e.g., suprathermal electrons) that ionize these same neutral species (especially on the nightside), and (3) subsequent ion-neutral photochemical reactions [e.g., *Fox*, 2004; *Fox and Sung*, 2001; *Fox and Yeager*, 2009]. The combined thermosphere-ionosphere system is regulated by these "topside" and "bottomside" forcing processes.

Properly addressing these coupling processes demands that simulations of the Martian thermosphere-ionosphere system be conducted in the context of a model domain that includes the Martian lower and middle atmosphere (~0–100 km). Evidence of this lower to upper atmosphere coupling abounds in recent spacecraft data sets. For instance, aerobraking activities conducted by Mars Global Surveyor (MGS), Mars Odyssey (ODY), and Mars Reconnaissance Orbiter (MRO) all demonstrated a longitude-dependent behavior of the mass densities that was derived from accelerometer measurements. These variations are likely generated by a combination of planetary and tidal waves launched in the lower atmosphere that propagate to thermospheric heights [e.g., *Forbes et al.*, 2003; *Wilson*, 2002; *Moudden and Forbes*, 2008, 2010]. In addition, Mars Odyssey accelerometer data sets have been used to extract gravity wave characteristics of the lower thermosphere [e.g., *Fritts et al.*, 2006]. Sources of these gravity waves can be either topographic or nontopographic but are both likely generated in the lower atmosphere. Finally, the time evolution of the Noachis regional dust storm in 1997, as monitored by the MGS accelerometer and Thermal Emission Spectrometer (TES), reveals an initial expansion of the entire atmosphere (during storm onset), a corresponding enhancement of derived thermospheric densities and zonal winds at constant altitudes, followed by a slow dust storm decay and a relaxation of thermospheric densities and winds back to prestorm levels [e.g., *Keating et al.*, 1998; *Baird et al.*, 2007; *Bougher et al.*, 1999a, 2014a]. Each of these features strongly suggest that the Martian lower to upper atmosphere coupling strongly modifies the

otherwise solar-driven thermospheric structure. In addition, GCM simulations addressing the effects of dust storms in the Mars upper atmosphere have been recently studied with GCMs [*Bougher et al.*, 2014; *Medvedev et al.*, 2014] and predict thermospheric effects to be as strong as those in the lower atmosphere. Overall, observed thermospheric variability is likely linked to both dynamical and thermal coupling.

The Mars thermosphere-ionosphere (TI) system can also change dramatically over time since it is controlled by two highly variable components of the Sun's energy output: solar radiation (~0.1–200 nm) and the solar wind (see reviews by *Bougher et al.* [2002, 2008, 2014a]). The amount of soft X-ray (0.1–5 nm) and EUV (5–110 nm) solar radiation most responsible for heating the Mars thermosphere (and forming its ionosphere) varies significantly over time. These temporal variations result from the changing heliocentric distance (~1.38–1.67 AU), the planet's obliquity (determining the local season), and the changing solar radiation itself. Both solar rotation (~27 day periodic changes in the solar output) and solar cycle (~11 year periodic overall changes in solar output) variations of the solar X-ray and EUV fluxes are significant (up to factors of ~3 to 100, depending on the wavelength [*Woods and Rottman*, 2002]), producing dramatic variations in global thermospheric temperatures, composition, and winds [e.g., *Bougher et al.*, 2000, 2002, 2009; *Forbes et al.*, 2008], as well as ionospheric densities [e.g., *Fox*, 2004; *Venkateswara Rao et al.*, 2014]. Thus, significant variability of the Martian thermosphere and ionosphere system is directly linked to the variability of the solar EUV-UV fluxes received at Mars.

1.2. Thermosphere-Ionosphere Role in Volatile Escape

The Mars thermosphere-ionosphere (TI) system constitutes an important atmospheric reservoir that regulates present-day escape processes from the planet. Characterization of the TI system, and its spatial and temporal (e.g., solar cycle, seasonal, and diurnal) variability, is crucial to quantifying present-day volatile escape rates [*Chassefière and Leblanc*, 2004; *Bougher et al.*, 2014b].

Modern-day volatile escape processes from the Martian upper atmosphere include the following: (a) photochemical escape, largely resulting from dissociative recombination of molecular ions (e.g., O_2^+, N_2^+, and CO^+) forming energetic (hot) exospheric atoms (e.g., O, N, and C) with escape energies, (b) pickup ion escape, generated from gyrating ions produced in the corona (exosphere) that are dragged along by the solar wind magnetic field lines to partially escape (e.g., O^+ and H^+), (c) planetary ionospheric outflows (at lower altitudes), and (d) sputtering escape, where solar energetic particles and planet-directed pickup ions impact the neutral atmosphere with sufficient energy to eject thermospheric neutrals (e.g., CO_2, N_2, CO, and O) *Chassefière and Leblanc* [2004]. Each of these processes is ultimately dependent on the thermospheric densities and temperatures, and their variations driven by solar forcing and upward propagating waves. The embedded ionosphere is also subject to these same forcing mechanisms, along with the Mars crustal magnetic fields. Together these processes regulate the structure of the exosphere and the solar wind interaction. Thus, the proper simulation of the volatile escape processes at Mars requires the reliable simulation of the observed characteristics of the TI system, including its solar cycle, seasonal, and diurnal variability.

1.3. Martian Lower-to-Upper Atmosphere Model Development to Date

Properly addressing the coupling of the Martian lower, middle, and upper atmospheres is a difficult modeling task. Three-dimensional "whole atmosphere" models are ultimately required to capture all the physical processes (e.g., thermal, chemical, and dynamical) throughout the entire Mars atmosphere from the ground to just above the exobase (~0–250 km). Such a unified whole atmosphere model for Mars is similar to what is presently ongoing utilizing the Whole Atmosphere Community Climate Model terrestrial numerical model at the National Center for Atmospheric Research (NCAR) [e.g., *Liu et al.*, 2010; *Marsh et al.*, 2013; *Baumgaertner et al.*, 2013].

Two approaches have been employed to date to capture the physics of the entire Mars atmosphere (ground-to-exobase): (a) coupling of separate lower and upper atmosphere codes and (b) single-framework whole atmosphere codes [*Bougher et al.*, 2008]. Each approach has advantages and disadvantages. Coupling separate codes permits the unique physical processes (and timescales) of the lower and upper atmospheres to be addressed separately within the codes which can be optimized for this purpose. However, linking two separate models across an interface is not seamless. This refers to the lack of an exact match of thermal and dynamical processes (e.g., solar heating, IR cooling, diffusion, and numerical filtering) across this interface. Furthermore, both upward and downward coupling (e.g., constituent fluxes) are not easily activated across separate models. Whole atmosphere models remove the need for an artificial boundary between two separate codes while at the same time providing a continuous application of processes from

the ground to the exosphere. However, small time steps may be needed to accommodate disparate processes and their timescales throughout the model domain. Examples of the "coupled separate" model and single-framework whole atmosphere Mars model approaches are presented here to set the stage for the new ground-to-exosphere model being presented in this paper.

The coupled NASA Ames Mars general circulation model (MGCM) (0–90 km) and the NCAR Mars thermospheric general circulation model (MTGCM) (~70–300 km) constitute a numerical framework of two-independent three-dimensional codes linked across an interface at 1.32 μbars (~60–80 km) in the Mars atmosphere. This coupled configuration permits both thermal- and large-scale dynamical processes to be linked across the lower and upper atmospheres of Mars [*Bougher et al.*, 2004, 2006, 2009]. This two-model treatment is also designed to be a test bed for addressing coupling processes in advance of the development and validation of a comprehensive Mars whole atmosphere framework [*Bougher et al.*, 2008].

The MTGCM is a finite difference primitive equation model that self-consistently solves for time-dependent neutral temperatures, neutral-ion densities, and three component neutral winds over the Mars globe [e.g., *Bougher et al.*, 1999a, 1999b, 2000, 2002, 2004, 2006; *Bell et al.*, 2007]. The modern MTGCM code contains prognostic equations for the major neutral species (CO_2, CO, N_2, and O), selected minor neutral species (Ar, NO, $N(^4S)$, and O_2), and several photochemically produced ions (O_2^+, CO_2^+, O^+, CO^+, and NO^+). All fields are calculated on 33 pressure levels above 1.32 μbar, corresponding to altitudes from roughly 70 to 250 km, with a 5° resolution in latitude and longitude. The vertical coordinate is log pressure, with a vertical spacing of 0.5 scale heights. Key adjustable parameters that can be varied for MTGCM cases include the $F_{10.7}$ cm index (a proxy measured at the ground for solar EUV/UV fluxes), the heliocentric distance, and solar declination corresponding to Mars seasons. The MTGCM is driven from below by the NASA Ames Mars MGCM code [e.g., *Haberle et al.*, 1999] at the 1.32 μbar level (near 60–80 km). This detailed coupling (at every model time step) allows both the migrating and nonmigrating tides to cross the MTGCM lower boundary and the effects of the expansion and contraction of the Mars lower atmosphere (due to dust heating) to extend to the thermosphere. These two climate models are each run with a 2 min time step, with the MGCM exchanging fields with the MTGCM at this frequency. This coupled model configuration has been validated and used successfully to analyze an assortment of spacecraft observations, including thermosphere, ionosphere, and mesosphere data sets from MGS, ODY, MRO, and Mars Express [*Bougher et al.*, 1999a, 1999b, 2000, 2004, 2006, 2009; *McDunn et al.*, 2010; *Lillis et al.*, 2010]. However, this coupling configuration does not easily allow for downward coupling from the MTGCM to the MGCM code. Furthermore, an artificial boundary exists at the 1.32 μbar level between these two codes.

Alternatively, a whole atmosphere approach is adopted by the group at the Laboratoire de Meteorologie Dynamique (LMD). Presently, the LMD Mars general circulation model (LMD MGCM) solves the primitive equations of hydrodynamics on a sphere using a finite difference scheme based on the terrestrial Laboratoire de Meteorologie Dynamique Zoom (LMDZ) model [*Sadourny and Laval*, 1984]. It was originally extended up to about 80 km of altitude [*Forget et al.*, 1999], including all the relevant processes in the lower atmosphere, such as a realistic CO_2 condensation scheme, a water cycle [*Montmessin et al.*, 2004], and a photochemical model of the lower atmosphere [*Lefèvre et al.*, 2004]. Now the LMD MGCM has become a ground-to-exosphere model (0–240 km), which allows a self-consistent examination of the coupling between the lower and the upper atmosphere. The LMD MGCM is typically run with a 5.625° × 3.75° longitude-latitude grid. In the vertical, it uses a hybrid coordinate system (50 levels), with sigma coordinates in the lower atmosphere and pressure coordinates in the upper layers [*González-Galindo et al.*, 2009a, 2009b]. To simulate the upper atmosphere, the LMD MGCM includes a parameterization of the IR radiative transfer under Non Local Thermodynamic Equilibrium (NLTE) conditions, based on *Lopez-Valverde and Lopez-Puertas* [2001] and *López-Valverde et al.* [1998], a fast scheme to calculate the UV heating, a photochemical model especially developed for the study of the rarified Martian upper atmosphere [*González-Galindo et al.*, 2005], which considers the chemistry of the C, O, H, and N families and ionospheric reactions [*González-Galindo et al.*, 2008], and schemes for the molecular diffusion and viscosity [*Angelats i Coll et al.*, 2005; *González-Galindo et al.*, 2009a]. Recently, ionosphere chemistry was added to the LMD MGCM to reproduce the major photochemical ion species and their seasonal and diurnal variations [*González-Galindo et al.*, 2013].

Finally, a recent intercomparison of the LMD MGCM and the coupled MGCM-MTGCM codes was conducted that shows both models predict similar thermospheric temperatures when similar inputs (e.g., solar EUV-UV fluxes, cross sections, heating efficiencies, and near IR heating rates) are used [*González-Galindo et al.*, 2010].

1.4. Objectives of This Paper

The primary limitation of the coupled MGCM-MTGCM framework (i.e., artificial boundary) is now being overcome with the development and validation of a new single-framework whole atmosphere model (~0–250 km). The new Mars Global Ionosphere-Thermosphere Model (M-GITM) presented in this paper combines the terrestrial GITM framework [e.g., *Ridley et al.*, 2006; *Deng et al.*, 2008] with Mars fundamental physical parameters, ion-neutral chemistry, and key radiative processes in order to capture the basic observed features of the thermal, compositional, and dynamical structure of the Mars atmosphere from the ground to the exosphere [*Bougher et al.*, 2008, 2011a, 2011b; *Pawlowski et al.*, 2010, 2011, 2012]. The formulations and subroutines required for incorporation into the new M-GITM code are largely taken from existing NASA Ames Mars MGCM and NCAR MTGCM codes. Archived MGCM-MTGCM coupled simulations are also used to assist with M-GITM validation studies. M-GITM model validation is also conducted making use of key Martian spacecraft measurements (e.g., Viking to Mars Express), spanning both the lower and upper atmospheres. The main focus, however, is on thermosphere-ionosphere validation.

The objectives for this new M-GITM code are threefold: (a) to investigate the thermal and dynamical coupling of the Mars lower to upper atmospheres, (b) to provide an accurate representation of the observed thermosphere-ionosphere structure and its variations over the Mars seasons and solar cycle, and (c) to eventually link M-GITM with exosphere and plasma models in order to self-consistently address Mars atmospheric escape processes and determine modern escape rates. The M-GITM code is specifically constructed with this multiple model linkage in mind (see section 6). These objectives are designed to support MAVEN mission (2014–2016) activities.

An overview of this paper is as follows. Section 2 will briefly review the Mars spacecraft data sets that will be used to provide key atmospheric constraints for M-GITM. Section 3 details the new M-GITM model, specifically its formulation, included physics and inputs. Simulation results and comparisons with key spacecraft data sets are presented in section 4. A focused discussion about the characterization of the Mars upper atmosphere using the M-GITM code is given in section 5. A brief discussion of future features and planned improvements to the M-GITM code is given in section 6. And finally, section 7 summarizes key conclusions thus far making use of the M-GITM code.

2. Brief Review of Mars Spacecraft Data Sets: Key Constraints

Comprehensive reviews of the known structure of the Martian upper atmosphere were recently published or are presently in press [e.g., *Withers*, 2009; *Haider et al.*, 2011; *Bougher et al.*, 2014a]. These are wide ranging reviews that address many features of the thermosphere and ionosphere system. However, for this paper, we focus the discussion on those few key measurements to be used in the present M-GITM validation studies conducted and described below in section 4. These key data sets were selected based upon their uniqueness (e.g., Viking Landers 1 and 2), solar cycle plus seasonal sampling, and latitudinal versus local time coverage for altitudes largely below 250 km. Regardless, the existing constraints for the Martian thermosphere-ionosphere system are quite limited in their spatial and temporal extent. The MAVEN mission (2014–2016) and its planned measurements should change this situation tremendously.

2.1. Neutral Thermosphere (~100–250 km)

The composition of the Mars thermosphere, specifically neutral species densities, has only been directly measured with the Upper Atmosphere Mass Spectrometer (UAMS) instruments onboard the descending Viking Landers 1 and 2 [e.g., *Nier and McElroy*, 1977]. Densities (~115–200 km) for mid afternoon (solar zenith angle (SZA) ~ 44°) low-to-middle latitude locations were obtained, corresponding to solar minimum, near aphelion conditions.

By contrast, mass densities of the Mars thermosphere have been repeatedly measured by the accelerometers onboard MGS, ODY, and MRO spacecraft [*Keating et al.*, 1998, 2003, 2008; *Bougher et al.*, 1999a, 2006, 2014a; *Tolson et al.*, 1999, 2005, 2007, 2008; *Withers et al.*, 2003, 2006]. These different spacecraft accelerometers permitted density recovery over various altitude ranges spanning 95 to 170 km. The latitudinal and seasonal variations of these mass densities are quite significant. In addition, the Mars Express Spectroscopy for Investigation of Characteristics of the Atmosphere of Mars (SPICAM) stellar occultation data set provides densities (and also temperatures) in the Martian upper atmosphere (~60–130 km) [e.g., *Forget et al.*, 2009; *McDunn et al.*, 2010]. Mesopause temperatures (and heights) and their seasonal variations are notable features of this data set.

The combined solar cycle and seasonal variations in Martian dayside upper thermosphere (i.e., exosphere) temperatures have been the subject of considerable analysis and debate since the first Mariner 6, 7, and 9 ultraviolent spectrometer (UVS) measurements (1969–1972) and up to the recent Mars Express SPICAM UVS measurements (2004 to the present) [*Krasnopolsky*, 2010; *Huestis et al.*, 2010; *Bougher et al.*, 2014a]. The significant Mars eccentricity demands that both the solar cycle and seasonal variations in near exobase temperatures (T_{exo}) be considered together [*Bougher et al.*, 2000; *Bougher and Huestis*, 2010]. The most plentiful constraints for dayside low SZA (less than about 70°) T_{exo} are available for near solar minimum conditions [e.g., *Bougher et al.*, 2014a]. Such values have been extracted from the Viking Lander 1 (VL1) entry science data (~186 K) [*Nier and McElroy*, 1977; *Seiff and Kirk*, 1977], MGS accelerometer density scale heights (~200–230 K) [*Withers et al.*, 2006; *Keating et al.*, 2008], and from Mars Express SPICAM UVS airglow (CO_2^+ doublet) scale heights (201±10 K) [*Leblanc et al.*, 2006]. Conversely, solar moderate-to-maximum, toward perihelion T_{exo} values are currently estimated from Mariner 6-7 CO Cameron emissions (~315–350 K) [*Stewart et al.*, 1972], and Mariner 9 CO Cameron emissions (~325 K) [*Stewart*, 1972]. Additionally, MGS drag measurements near ~390 km [*Forbes et al.*, 2008; *Bougher et al.*, 2009] have also been used to constrain the exospheric temperatures. Detailed refinement of these estimates making use of Mars Express SPICAM dayside airglow measurements (CO_2^+ doublet and CO Cameron emissions) and new analysis techniques is being developed [e.g., *Leblanc et al.*, 2006; *Huestis et al.*, 2010; *Stiepen et al.*, 2014].

Table 1 from *Bougher et al.* [2002] provides an overview of dayside T_{exo} values extracted from various observations over the last 45 years. These tabulated T_{exo} values are compared with corresponding M-GITM predictions in section 4.

2.2. Lower Ionosphere (~100–250 km)

Comprehensive reviews of the Martian ionosphere data sets are given in *Withers* [2009] and *Haider et al.* [2011]. Retarding Potential Analyzers (RPA) were used to measure ion densities on the Viking Landers [*Hanson et al.*, 1977]. Radio Occultation measurements have been obtained by various spacecraft, including the Mariners, Viking, MGS, and Mars Express [*Withers*, 2009; *Haider et al.*, 2011]. Lastly ionospheric sounding is still being conducted by the Mars Express Mars Advanced Radar for Subsurface and Ionosphere Sounding (MARSIS) instrument [*Gurnett et al.*, 2005; *Morgan et al.*, 2008]. While electron density measurements are numerous, the composition of the Mars ionosphere, specifically thermal ion species densities, has only been directly measured with the RPA instruments onboard the descending Viking Landers 1 and 2 [*Hanson et al.*, 1977].

2.3. Middle Atmosphere(≤90 km)

This is not primarily a paper focused upon the Mars lower-middle atmosphere. However, climatological constraints for this atmospheric region are needed to validate the M-GITM simulated temperature structure. The MRO Mars Climate Sounder (MCS) instrument has been operating nearly continuously since September 2006, spanning more than four Martian years (MY = 28–31) [e.g., *McCleese*, 2008; *Kleinböhl et al.*, 2009, 2011; *McDunn et al.*, 2013]. Hence, MCS retrieved (version 4.0) temperatures (~0–90 km) are utilized (as a function of season, latitude, and local time) to provide constraints for validating the basic features of the M-GITM temperature structure below ~80–90 km.

3. Mars Global Ionosphere-Thermosphere Model: Formulation and Inputs

3.1. M-GITM Broad Overview

The GITM code is a 3-D spherical model that was originally developed to simulate the terrestrial thermosphere-ionosphere system (~100–500 km) using an altitude-based vertical coordinate [*Ridley et al.*, 2006]. This allows for the relaxation of the assumption of hydrostatic equilibrium and enables the model to resolve sound and gravity waves in both the vertical and horizontal directions. GITM solves for the bulk horizontal neutral winds, while in the vertical direction, the momentum equation for each major species is solved and the bulk vertical wind is specified as a mass density weighted average of the individual vertical velocities. The model is fully parallel and utilizes a block-based 2-D (latitude and longitude) domain decomposition that allows the model to have a flexible horizontal resolution that can be specified at run time. For parallel computation, GITM uses the message passing interface standard to allow for platform independence when passing information between 2-D blocks. The Earth GITM code is typically used to address neutral, ion, and electron temperatures, composition, and wind fields from ~100 to 500 km for numerous

Table 1. Chemical Reactions and Associated Rates in Mars-GITM

Reaction Number	Chemical Reaction	Rate ($m^3\ s^{-1}$)
	Primary Photolysis (Now) /Particle Impact (Later)	
(R1)	$N_2 + h\nu, e^- \rightarrow N(^4S) + N(^2D)$	
(R2)	$N_2 + h\nu, e^- \rightarrow N_2^+$	
(R3)	$CO_2 + h\nu, e^- \rightarrow CO_2^+$	
(R4)	$CO_2 + h\nu, e^- \rightarrow CO + O$	
(R5)	$O_2 + h\nu, e^- \rightarrow O_2^+$	
(R6)	$O_2 + h\nu, e^- \rightarrow O + O$	
(R7)	$O + h\nu, e^- \rightarrow O^+$	
	Neutral Bimolecular Chemistry	
(R8)	$N(^2D) + CO_2 \rightarrow NO + CO$	3.60×10^{-19}
(R9)	$N(^2D) + CO \rightarrow N(^4S) + CO$	1.92×10^{-18}
(R10)	$N(^2D) + O \rightarrow N(^4S) + O$	6.9×10^{-19}
(R11)	$N(^2D) + O_2 \rightarrow N(^4S) + O_2$	$9.70 \times 10^{-18}\ e^{-185/T_n}$
(R12)	$N(^2D) + N_2 \rightarrow N(^4S) + N_2$	1.70×10^{-20}
(R13)	$NO + N(^4S) \rightarrow N_2 + O$	$2.50 \times 10^{-16}\ (T_n/300)^{0.5}\ e^{-600/T_n}$
(R14)	$N(^4S) + O \rightarrow NO + h\nu$	$1.90 \times 10^{-23}\ (300/T_n)^{0.5}\ \left(1.0 - \frac{0.57}{\sqrt{T_n}}\right)$
	Ion-Neutral Chemistry	
(R15)	$CO_2^+ + O \rightarrow O_2^+ + CO$	1.64×10^{-16}
(R16)	$CO_2^+ + O \rightarrow O^+ + CO_2$	9.60×10^{-17}
(R17)	$O^+ + CO_2 \rightarrow O_2^+ + CO$	1.10×10^{-15}
(R18)	$N_2^+ + CO_2 \rightarrow CO_2^+ + N_2$	$9.00 \times 10^{-17}\ (300.0/T_i)^{0.23}$
(R19)	$N_2^+ + O \rightarrow NO^+ + N(^4S)$	$1.33 \times 10^{-16}\ (300.0/T_i)^{0.44}$
(R20)	$O^+ + N_2 \rightarrow NO^+ + N(^4S)$	$1.20 \times 10^{-18}\ (300.0/T_i)^{0.45}$
(R21)	$O_2^+ + N(^4S) \rightarrow NO^+ + O$	1.00×10^{-16}
	Electron Recombination Chemistry	
(R22)	$N_2^+ + e^- \rightarrow 2\ (0.25\ N(^4S) + 0.75\ N(^2D))$	$1.01 \times 10^{-13}\ (300.0/T_e)^{0.39}$
(R23)	$O_2^+ + e^- \rightarrow 2O$	$1.95 \times 10^{-13}\ (300.0/T_e)^{0.70}$
(R24)	$CO_2^+ + e^- \rightarrow CO + O$	$3.50 \times 10^{-13}\ (300.0/T_e)^{0.50}$
(R25)	$NO^+ + e^- \rightarrow O + N(^2D)$	$3.40 \times 10^{-13}\ (300.0/T_e)^{0.50}$
(R26)	$NO^+ + e^- \rightarrow O + N(^4S)$	$0.60 \times 10^{-13}\ (300.0/T_e)^{0.50}$
	Termolecular Neutral Chemistry	
(R27)	$O + O + CO_2 \rightarrow O_2 + CO_2$	2.75×10^{-44}
(R28)	$O + O_2 + CO_2 \rightarrow (\text{Not Tracked}) + CO_2$	1.35×10^{-45}
(R29)	$O + CO + CO_2 \rightarrow 2\,CO_2$	$6.50 \times 10^{-45}\ e^{-2180/T_n}$
(R30)	$O + N(^4S) + CO_2 \rightarrow NO + CO_2$	$2.0 \times 10^{-44}\ (300.0/T_n)^{0.50}$

space weather modeling applications [e.g., *Ridley et al.*, 2006; *Deng et al.*, 2008; *Pawlowski and Ridley*, 2008, 2009a, 2009b].

Unlike at Earth, M-GITM simulates the conditions of the Martian atmosphere from the surface all the way to the exosphere (~0–250 km). The formulations and subroutines required for incorporation into the new M-GITM code have largely been taken from existing Mars GCM codes that have been developed and validated elsewhere (see review by *Bougher et al.* [2008]).

M-GITM currently solves for neutral and ion densities, as well as neutral temperatures and winds. Key neutral species presently include the following: CO_2, CO, O, N_2, O_2, and Ar. Future minor species will include the following: $N(^4S)$, $N(^2D)$, NO, H, He, and H_2. Five key photochemical ion species currently include the following: O^+, O_2^+, CO_2^+, N_2^+, and NO^+. The M-GITM code can be run for various horizontal and vertical resolutions. Typically, production runs are conducted for a $5 \times 5°$ regular horizontal grid, with a constant 2.5 km

vertical resolution (~0.25 scale height). However, M-GITM can also use a stretched altitude grid below ~80 when surface topography is included.

3.2. Governing Equations

The M-GITM code uses the same basic set of Navier-Stokes equations found in the terrestrial GITM code for the neutral temperatures, densities, and winds [*Ridley et al.*, 2006; *Bell et al.*, 2011a, 2011b]. The radial distance is the vertical coordinate, and like its Earth predecessor, Mars GITM solves the Navier-Stokes equations in the radial direction separately from the horizontal directions consistent with other existing GCMs [e.g., *Roble et al.*, 1988; *Mueller-Wodarg et al.*, 2000].

The general GITM framework solves these fluid equations in a 3-D spherical coordinate system while relaxing the assumption of hydrostatic equilibrium. This means that in the radial direction, the model assumes that each neutral species possesses its own continuity and momentum equations that are solved in the vertical direction self-consistently. This procedure, as demonstrated by *Deng et al.* [2008] and *Bell et al.* [2014], allows for significant vertical accelerations and velocities to potentially develop, especially in areas of highly localized heating (e.g., due to Joule heating or auroral particle precipitation). For Mars, strong localized heating (possibly resulting in significant vertical velocities) may also be provided by solar energetic particles and O^+ precipitation events under extreme solar wind conditions [*Fang et al.*, 2013]. Typically, the simulated neutral atmosphere is in hydrostatic balance for nominal driving conditions. Furthermore, the GITM framework assumes that all neutral species share a single bulk temperature and energy equation [*Ridley et al.*, 2006]. In the horizontal directions (i.e., latitude and longitude), the framework assumes that all species share the same zonal and meridional bulk winds in addition to the same background temperature (consistent with the collision-dominated approximation). Finally, in order to accommodate the solution for the nonhydrostatic atmosphere, GITM uses an altitude-based vertical coordinate as opposed to a pressure-based coordinate. The relaxation of the assumption of hydrostatic balance and separate vertical momentum equations for each species makes the GITM codes unlike many other global circulation models (GCMs) of planetary ionosphere-thermosphere regions (see review by *Bougher et al.* [2008]).

The detailed Navier-Stokes equations used by GITM are outlined in *Ridley et al.* [2006]. Nevertheless, we present the equations associated with the vertical component of the neutral winds in order to highlight the terms that bring nonhydrostatic effects to the system. The vertical continuity equation is

$$\frac{\partial \mathcal{N}_s}{\partial t} + \frac{\partial u_{r,s}}{\partial r} + \frac{2u_{r,s}}{r} + u_{r,s}\frac{\partial \mathcal{N}_s}{\partial r} = \frac{1}{N_s}\mathcal{L}_s, \tag{1}$$

where the subscript r denotes the radial component, $\mathcal{N}_s$ is the natural log of the neutral density of species s, N_s is the neutral density of species s, $u_{r,s}$ is the radial neutral velocity of species s, and $\mathcal{L}_s$ are the chemical source and loss terms, which are described in section 3.6.2. Eddy and molecular diffusion are included in the vertical momentum equation (via their vertical velocities). The $\frac{2u_{r,s}}{r}$ term comes from the radial divergence of the radial component of the velocity.

The corresponding vertical momentum equation is

$$\frac{\partial u_{r,s}}{\partial t} + u_{r,s}\frac{\partial u_{r,s}}{\partial r} + \frac{u_\theta}{r}\frac{\partial u_{r,s}}{\partial \theta} + \frac{u_\phi}{r\cos\theta}\frac{\partial u_{r,s}}{\partial \phi} + \frac{k}{M_s}\frac{\partial T}{\partial r} + T\frac{k}{M_s}\frac{\partial \mathcal{N}_s}{\partial r} = g + F_s + \frac{u_\theta^2 + u_\phi^2}{r} + \cos^2\theta\Omega^2 r + 2\cos\theta\Omega u_\phi, \tag{2}$$

where θ is the north latitude, ϕ is the east longitude, u_θ is the northward neutral velocity, u_ϕ is the eastward neutral velocity, Ω is the angular velocity of Mars, T is neutral temperature, g is gravity (altitude dependent), k is the Boltzmann constant, M_s is the molecular weight of species s, and F_s are the source and loss terms (accelerations) due to ion-neutral friction and neutral-neutral friction when each constituent is solved independently (see section 3.6.3). This is where molecular and eddy diffusion are incorporated; eddy diffusion is discussed in section 3.6.5. The last two terms on the right side are the centrifugal and Coriolis forces. The $\frac{u_\theta^2+u_\phi^2}{r}$ term is due to the spherical geometry and causes the horizontal winds to "lift off" from the curved surface of the planet. For small horizontal and vertical velocities (i.e., typical under steady state assumptions), this equation is reduced to that consistent with hydrostatic balance [*Deng et al.*, 2008; *Bell et al.*, 2014].

Solution of the Navier-Stokes equations in the vertical direction is typically difficult because the vertical gradient in the number density is quite strong. For this reason, the natural logarithm of the number densities are used as the primitive variables in the GITM framework. This is done because, while the density varies

exponentially with altitude, the logarithm of the density varies nearly linearly, which is easier to solve numerically. After the advection is complete and these fundamental equations have been solved within the code, source and loss terms (e.g., chemical sources and losses, solar heating, radiative cooling, and viscosity) are added.

In the ionosphere, the equations are also separated into the horizontal and vertical directions. The ion momentum equation is written as

$$\rho_i \frac{\partial \mathbf{v}}{\partial t} = -\nabla(P_i + P_e) + \rho_i \mathbf{g} - \rho_i \nu_{in}(\mathbf{v} - \mathbf{u}), \tag{3}$$

where ρ_i is the ion mass density, $\mathbf{v}$ is the vector ion velocity, $\mathbf{u}$ is the vector neutral velocity, P_i and P_e are the ion and electron pressures, and ν_{in} is the ion-neutral collision frequency. We do not currently solve for an external electric field or include the crustal magnetic fields in M-GITM. In the model, we assume that the left-hand side of equation (3) is negligible (zero time tendency) relative to the other terms. This means that the momentum equation can be simplified to be a balance between the drag due to the neutrals, gravity, and the polarization electric field:

$$\mathbf{v} = \mathbf{u} + \frac{\rho_i \mathbf{g} - \nabla(P_i + P_e)}{\rho_i \nu_{\text{in}}}. \tag{4}$$

For this paper, we describe a photochemical ionosphere (only), for which $\mathbf{v} = 0.0$. Presently, this limits the validity of the simulated M-GITM ionosphere to altitudes below ~200 km, as described in section 3.6.2 [e.g., *Bougher et al.*, 2014a]. Future publications will specifically address ionospheric transport. Lastly, the ion and electron temperatures are not calculated self-consistently within the solver at this time. Instead, the temperatures are specified using the empirical formulation by *Fox et al.* [1993] which assumes that the electron temperature is equal to the neutral temperature below 130 km and increases in an exponential manner above, while the ion temperature is assumed to be equal to the neutral temperature below 180 km and between the electron and neutral temperatures at higher altitudes.

3.3. Boundary Conditions, Steady State, and Filtering

As discussed in *Ridley et al.* [2006], GITM uses two layers of ghost cells outside the physical cells to specify boundary conditions for all three dimensions. Boundary conditions are needed in latitude and longitude to facilitate message passing between individual decomposition blocks that are sent to parallel processors. In the vertical direction, M-GITM neutral densities are specified at the lower boundary (i.e., at the surface), whereas the neutral density gradients are allowed to be continuous at the top of the model (i.e., at the exobase). The exobase neutral density gradients are consistent with molecular diffusion and ensure that all species adopt a mass-specific hydrostatic profile. Similarly, temperatures at the lower boundary are specified according to empirically derived diurnal and seasonal variations, while neutral temperature gradients are specified to be zero at the upper boundary, consistent with the exobase approximation. Finally, vertical winds are specified to be zero at the surface and are assumed to have a zero gradient at the upper boundary.

It is important to recognize that the density at the lower boundary is forced to be in a quasi-hydrostatic equilibrium, where gravity, pressure, and the Coriolis and centrifugal terms are in balance. To make this possible, the first ghost cell in the boundary is held fixed at its initialized value and the second ghost cell is allowed to change in order to put the boundary in equilibrium with the first real cell.

Steady state conditions are achieved after roughly 20 Martian solar days (sols) of integration, and the initial conditions no longer have an impact on the simulated fields. M-GITM also utilizes a Rayleigh drag term that is introduced into the vertical momentum equation to provide continuous and smooth winds near the planetary surface. Introduction of planetary boundary layer physics will remove the need for this artificial viscosity term, but it is similar in structure to that employed by other models near the computational boundary [e.g., *Dowling et al.*, 1998].

3.4. Model Timing

Mars time is measured (with respect to the Earth clock) based upon the precise Earth time that Mars encountered its Vernal Equinox (at local midnight) on 14 July 1998. Once an Earth date and time is selected at run time, an electronic ephemeris is utilized to extract the Mars season (solar longitude (Ls)), its heliocentric distance, and the declination of the Sun. These parameters are then used for scaling solar fluxes (visible, IR, UV, and EUV) to the Mars location, and rotating Mars to the correct Mars Universal Time (UT) (i.e., local time

versus longitude position). Recall that the Mars sol is about 40 min longer than the Earth day. This scheme is beneficial for matching the Mars observing dates with the correct solar, orbital, and seasonal parameters. However, it is not ideal for specifying (at run time) an integral multiple number of Mars sols for M-GITM integration. Instead, the user must keep track of the integral Mars sols and request outputs at the Earth UT that matches Mars UT = 0. This inconvenience is small compared to the easy method for making M-GITM simulations that match observations for a given Earth date and time.

3.5. Lower Atmosphere Physics ($\leq$ 80 km)

While the core solver of M-GITM is basically the same solver that is utilized within the Earth and Titan GITM codes, the planet-specific physics are included as source terms.

3.5.1. Correlated-*k* Radiative Transfer Code

For the Mars lower atmosphere (0–80 km), a radiative transfer (RT) code was adapted from the NASA Ames MGCM [*Haberle et al.*, 2003] for incorporation into M-GITM. This provides solar heating (long and short wavelength), seasonally variable aerosol heating, and CO_2 15 μm cooling in the Local Thermodynamic Equilibrium (LTE) region of the Mars atmosphere (below ~80 km). The radiation code presently being used for Mars is based on a two-stream solution to the radiative transfer scheme with CO_2 and water vapor opacities calculated using a correlated-*k* approach. The two-stream solution is generalized for solar and infrared radiation with scattering based on the δ-Eddington approximation at visible wavelengths and the hemispheric mean approximation at infrared wavelengths [*Toon et al.*, 1989]. This Mars code has correlated-*ks* for CO_2 and water vapor for 12 spectral bands (between 0.3 to 250 μm) tailored for the Mars CO_2 and water vapor atmosphere (five = infrared and seven = visible bands) [*Haberle et al.*, 2003]. The returned values from this radiation code are visible and IR fluxes, from which heating and 15 μm cooling rates can be derived for use by the M-GITM code. Application of this Mars correlated-*k* code is limited to pressures greater than 1.0 nbar (below ~115–125 km, depending on season).

The correlated-*ks* for these intervals are generated from a line-by-line code using the High Temperature Molecular Spectroscopic Database (HITEMP) database from High Resolution Transmission Database (HITRAN) for CO_2 and a version of the Schwenke database (to include lines too weak to appear in HITRAN) for H_2O. In both cases, line widths are adjusted to represent CO_2 broadening. A Voigt profile is used at low pressures, and a Lorentz profile is used at high pressures. The line widths are extended at high pressures so as to include all significant absorption. The line-by-line calculations were then windowed and sorted to produce the *k* coefficients. The code uses a Gauss scheme of 8×8 points in each spectral interval with the dividing point at 0.95 to extract the actual coefficients from the sorted probability distribution. The *k* coefficients have been computed for a range of pressures, temperatures, and relative humidities that allows us to simulate past as well as present Martian climates. CO_2 pressure-induced transitions near 7 and beyond 20 μm are included using parameterizations developed by *Pollack et al.* [1980], *Kasting et al.* [1984], and *Mischna et al.* [2012].

For aerosols, the correlated-*k* package calculates the appropriate scattering parameters using a Mie code. In fixed dust runs, we directly use the *Ockert-Bell et al.* [1997] scattering properties in the visible. In the infrared we use a Mie code to calculate the scattering properties using the wavelength-dependent refractive index of *Forget et al.* [1999] and a lognormal size distribution with a mean size and variance of 2.7 μm and 0.38, respectively.

3.5.2. Mars Surface Temperature Distribution

In addition, a simple (fast) formulation for Mars surface temperatures was implemented and tested within the M-GITM code. This scheme makes use of global empirical maps of albedo and thermal inertia (see section 3.7) in the surface temperature prescription. Overall, this fast scheme is based upon Mars empirical temperatures and is shown to match seasonal, latitude, and local time variations in temperatures reasonably well. These surface temperatures are needed for proper computations by the correlated-*k* radiative transfer code.

3.5.3. Gravity Wave Momentum Deposition Formulation

A simplified gravity wave momentum deposition formulation was recently coded into M-GITM, similar to the scheme used by *Palmer et al.* [1986] and *Forget et al.* [1999]. This scheme is currently being tested within the M-GITM code in order to examine the role gravity waves play in regulating zonal and meridional winds (and the corresponding winter polar warming temperatures) in the lower and middle atmospheres, and their impact on the upper atmosphere (above ~ 80–90 km). Later versions of the M-GITM code will fully implement and validate this gravity wave scheme. However, no gravity wave momentum deposition is included in the current simulations presented in this paper.

3.6. Upper Atmosphere Physics (~80–250 km)

3.6.1. EUV-UV Heating, Dissociation, and Ionization

The terrestrial GITM thermospheric EUV-UV heating routines have been modified for a CO_2 atmosphere, by incorporating an expanded set of cross sections and yields for CO_2 and CO, much like the MTGCM code [*Bougher et al.*, 1999b, 2000]. The solar fluxes and cross sections (0.1 to 175.0 nm) that are included span 59 wavelength intervals: (a) 7 bins (0.1 to 5.0 nm) for soft X-rays, (b) 37 bins (5–105 nm) for EUV, (c) 1 bin for Ly α, (d) 6 bins (105–135 nm) for FUV, and (f) 8 bins (130–175 nm) for the Schumann Runge continuum. This combined solar flux spectrum, and various techniques for its prescription, is presently provided from the Solomon solar flux model commonly used in terrestrial thermospheric general circulation model simulations [e.g., *Ridley et al.*, 2006]. Cross sections (and yields) for EUV bins are adopted (partially) from *Schunk and Nagy* [2009]. For the present application, daily $F_{10.7}$ and 81 day averaged $F_{10.7A}$ indices are set equal in order to generate reference fluxes for typical solar conditions found at $F_{10.7}$ centimeter indices of 200, 130, and 70. These indices are generally consistent with solar maximum (SMAX), solar moderate (SMED), and solar minimum (SMIN) conditions, respectively. Additionally, M-GITM is capable of using Earth-based data from the Solar Extreme Ultraviolet Experiment [*Woods et al.*, 2005] or EUV Variability Explorer (EVE) [*Woods et al.*, 2010] instruments as well as model results from the Flare Irradiance Spectral Model [*Chamberlin et al.*, 2008] to drive the EUV heating.

This solar flux model and corresponding cross sections enable the computation of the in situ heating (EUV-UV), dissociation rates (e.g., CO_2, O_2, and N_2) and ionization rates (e.g., CO_2, O_2, O, and N_2) spanning ~80 to 250 km. These calculations are done at every model time step. An EUV-UV heating efficiency of 18% is used, the lower limit of that simulated offline in detailed energy tracking calculations [*Fox et al.*, 1996; *Huestis et al.*, 2008].

3.6.2. Ion-Neutral Chemical Reactions and Rates

Table 1 presents a comprehensive set of 30+ key ion-neutral chemical reactions and rates that have been incorporated into the M-GITM code [e.g., *Fox and Sung*, 2001], based upon those used previously in the modern Mars thermospheric general circulation model (MTGCM) [e.g., *Bougher et al.*, 2004, 2006, 2009]. In order to calculate chemical sources and losses, M-GITM utilizes a subcycling technique whereby several chemical time steps may be taken during a single advective time step. At this stage, M-GITM assumes photochemical equilibrium when solving for the dayside ionosphere (above ~80 km). Future upgrades will address the incorporation of ion-transport and ambipolar diffusion. Thus, the M-GITM dayside photochemical ionosphere is a valid approximation below ~200 km [*Zhang et al.*, 1990; *Withers et al.*, 2010; *Bougher et al.*, 2014a]. Ion dynamics has recently been shown to be important at higher altitudes [*Chaufray et al.*, 2014].

3.6.3. Multiconstituent Molecular Diffusion: Neutral-Neutral

Neutral-neutral friction in the vertical direction is included as a forcing term within the M-GITM model following the formulation of *Colegrove et al.* [1966]:

$$\mathcal{F}_s = \frac{kT}{M_s} \sum_{q \neq s} \frac{n_q}{n D_{qs}} (u_{r,q} - u_{r,s}) \tag{5}$$

where $u_{r,q}$ is the radial component of the neutral velocity of species q, n_q is the density of species q, and n is the background neutral density. D_{qs} represents the binary molecular diffusion coefficient between the s and q constituents, as formulated by *Banks and Kockarts* [1973]

$$D_{sq} = \frac{A_{sq} T^b}{N}. \tag{6}$$

The values for the A_{sq} coefficients and b exponents are taken from several references in the literature [e.g., *Banks and Kockarts*, 1973; *Mason and Marrero*, 1970; *Massman*, 1998; *Colegrove et al.*, 1966]. Finally, this $\mathcal{F}_s$ neutral-neutral friction term is one element of the combined neutral-neutral plus ion-neutral term (F_s) in equation (2).

3.6.4. Specific Heat, Thermal Conduction, and Molecular Viscosity

Calculations of the specific heat, thermal conduction, and molecular viscosity are based upon standard aeronomical formulations that have been used before in the MTGCM code [*Bougher et al.*, 1999b, 2000]. They are all based upon the *Banks and Kockarts* [1973] formulations for a mixture of gases (CO_2, CO, N_2, and O) as a function of location around the globe.

3.6.5. Eddy Diffusion and Viscosity

The eddy diffusion coefficient is specified according to the following formulation. First, the altitude level is identified corresponding to the asymptotic upper boundary (in pressure) for eddy diffusion (extract density N_{max} for this level). We define this level at $p = 1.26$ nbar pressure level, where *Stewart* [1987] defines the homopause and the subsolar ionospheric peak (F_1 peak) altitude is located. Then,

$$\kappa_{eddy}(z) = \kappa_{max}\sqrt{\frac{N_{max}}{N(z)}}, \tag{7}$$

where $\kappa_{eddy}(z) = \kappa_{max}$ for $N(z) > N_{max}$ and κ_{min} (a minimum value) is set. Also, $\kappa_{max} = 1 \times 10^7$ cm^2/s and $\kappa_{min} = 5.0 \times 10^6$ cm^2/s. This is a standard formulation for the eddy diffusion coefficient used in many 1-D models. However, the adjustable κ_{max} and κ_{min} values at Mars differ substantially between 1-D and 3-D model simulations [*Bougher et al.*, 1999b, 2000]. Previous model studies suggest that the global thermospheric circulation actually serves to significantly redistribute species vertically and horizontally [*Bougher et al.*, 1999b, 2000], such that reduced small-scale mixing (approximated by eddy diffusion) is needed in global models, compared to 1-D models [*Nier and McElroy*, 1977; *Rodrigo et al.*, 1990; *Krasnopolsky*, 2010]. The latter typically make use of κ_{max} values that range from 5 to 30 $\times 10^7$ cm^2/s (at a homopause altitude near ~130 km).

3.6.6. NLTE CO_2 Cooling and Near IR Heating

For the Mars upper atmosphere (~80 to 250 km), an existing fast formulation for NLTE CO_2 15 μm cooling was implemented into the M-GITM code [e.g., *López-Valverde et al.*, 1998; *Bougher et al.*, 2006]. This scheme has been modified to permit the dynamical interaction of simulated atomic O within the cooling rate calculation [*Bougher et al.*, 2006]. In addition, a correction for NLTE near IR heating rates (~80–120 km) was implemented using an upward extension of the same correlated-*k* radiation code. This NLTE to LTE correction, for application to the simulated LTE heating rates above ~80 km, is patterned after that presented by *López-Valverde et al.* [1998].

The relative importance of NLTE CO_2 15 μm cooling in the energy budget of the Mars upper atmosphere is still uncertain and depends upon three main factors: (a) the atomic oxygen abundance, (b) the CO_2 abundance, and (c) the collision excitation rate coefficient [*Bougher et al.*, 2014a]. Presently for Mars, the thermospheric O abundance is poorly measured, and few thermal measurements of the upper atmosphere exist to constrain 15 μm cooling rates. Also, the value of O-CO_2 quenching rate coefficient (linked to the collision excitation rate coefficient by detailed balance) is presently set at 3.0×10^{-12} cm^3 s^{-1} at 300 K, midway between conflicting laboratory measured and radiance model-derived values for Earth's upper atmosphere (see reviews by *Huestis et al.* [2008] and *Bougher et al.* [2014a]). Lastly, the formulation for NLTE CO_2 15 μm cooling presently adapted for use in the M-GITM code is in need of refinement [*López-Valverde et al.*, 2006] in order to improve the calculation of Mars mesopause temperatures and heights [*Forget et al.*, 2009; *McDunn et al.*, 2010]. This refinement will be addressed in a subsequent M-GITM paper and patterned after that used in *González-Galindo et al.* [2013].

3.6.7. NLTE O 63 μm Cooling

The NLTE O 63 μm cooling is due to the O(^{3}P) emission from the fine structure of atomic oxygen. This IR cooling has a minor contribution to the energy budget of the terrestrial thermosphere [*Roble*, 1995]. Here the LTE (optically thin) formulation is found in *Banks and Kockarts* [1973]. An approximation for NLTE effects is provided by *Roble et al.* [1987], for which the LTE 63 μm cooling rate is reduced by a factor of 2. The same NLTE formulation scheme is used for the Martian upper atmosphere, where it is also expected that its contribution to the energy budget is small.

3.7. Input Data Sets

At the surface, global empirical maps of albedo and thermal inertia are supplied to the correlated-*k* radiation calculations to provide accurate global variations of these quantities. The data sets utilized are adopted from those presently used in the NASA Ames MGCM [*Haberle et al.*, 2003, 1999].

In addition, vertical integrated dust opacity (τ) and distributions (horizontal) are typically prescribed based upon empirical dust opacity maps obtained from several Martian years of MGS/TES, and Odyssey/Thermal Emission Imaging System measurements [*Smith*, 2004, 2009; *McDunn et al.*, 2010]. Alternatively, globally averaged (and annual-averaged) dust opacities can be specified for diagnostic studies; this approach was used for the present M-GITM simulations. Likewise, the vertical distribution of dust is typically parameterized

Table 2. Summary of M-GITM Metrics of Key Parameters Used for Model Validation[a]

Case	T_{max} (K) (LT = 3)	$\|v\|_{max}$ (m/s) (ET) (MT)	Diurnal Ratios (CO_2) (O)	$O/CO_2 = 1.0$ (km)	$F1$ peak (hmax, km) (Nmax,1/m^3)	$F1$ peak (O/CO_2) (O_2^+/CO_2^+)
EQU/	215	+250	600	200	125	1.8%
SMIN	120	−250	6.7		1.58	4.5
EQU/	350	+350	950	240	125	2.5%
SMAX	134	−350	6.0		2.51	5.0
APH/	190	+170	8000	190	120	1.8%
SMIN	104	−200	5.6		1.25	6.0
PER/	390	+310	20000	240–250	128	3.1%
SMAX	114	−410	6.92		3.1	4.0

[a]ET = evening terminator; MT = morning terminator. $F1$ peak quantities and $O/CO_2 = 1$ altitudes given at low SZAs. Diurnal ratios given at 200 km. $F1$ peak magnitudes are scaled by 1×10^{11}.

using the Conrath scheme [*Conrath*, 1975], for which a Conrath parameter (CR) is specified. This scheme yields well-mixed vertical distributions of dust below a certain altitude and an exponential decay of dust at higher altitudes. For the M-GITM simulations conducted for this paper, the horizontal dust opacities (visible) have been prescribed to be an annual-averaged (and global-averaged) value of 0.5. The vertical extent of the dust is prescribed using a Conrath parameter of 0.003, which implies that dust is well mixed up to ~ 50 km, and exponentially decreasing above this altitude. Such a global-averaged (an annual-averaged) dust scenario likely overestimates the role of dust heating during the nondusty seasons and underestimates it during the rest of the Martian year. However, this static dust prescription does aid the analysis of solar cycle and seasonal forcing of the upper atmosphere.

The coordinate system within M-GITM has been modified to include the use of topography measurements provided by the Mars Orbiter Laser Altimeter (MOLA) instrument onboard MGS [*Smith and Zuber*, 1996]. The data are provided at 1/4° by 1/4° resolution and, upon being read in to the model, are interpolated to the M-GITM grid. Two modifications were made to the core numerics of M-GITM to accommodate a terrain-following coordinate system: (1) the vertical solver was modified to allow for the inclusion of the topography and (2) vertical boundary conditions were altered. For the M-GITM simulations conducted for this paper, the topography was turned off; i.e., future M-GITM simulations will incorporate topography and its effects. See sections 6 and 7 for further discussion.

4. Mars GITM Simulation Results and Comparisons With Data Sets

Initial M-GITM simulations indicate this extended model is stable and convergent and captures the basic observed ground-to-exobase temperatures, major upper atmosphere neutral and ion composition, and expected basic wind structures throughout the Mars atmosphere [e.g., *Pawlowski et al.*, 2010; *Bougher et al.*, 2011b]. M-GITM ground-to-exobase (0–250 km) simulations are run for ~20 sols each, permitting both spin-up of the global dynamics (from a static initial atmosphere) and a smooth transition to steady state conditions as the specific season of interest is approached. Model simulations and validation studies thus far have focused upon calculations for three seasons (Ls = 90, 180, and 270) and for solar minimum ($F_{10.7}$ = 70), solar moderate ($F_{10.7}$ = 130), and solar maximum ($F_{10.7}$ = 200) conditions.

Most of the model validation discussion in this section is focused upon upper atmosphere model results and corresponding spacecraft data sets; key upper atmosphere metrics are summarized in Table 2. However, one section is devoted to lower-middle atmosphere results and comparisons to MRO/MCS dayside measured temperatures. The purpose here is to provide an overview of the lower atmosphere structure being

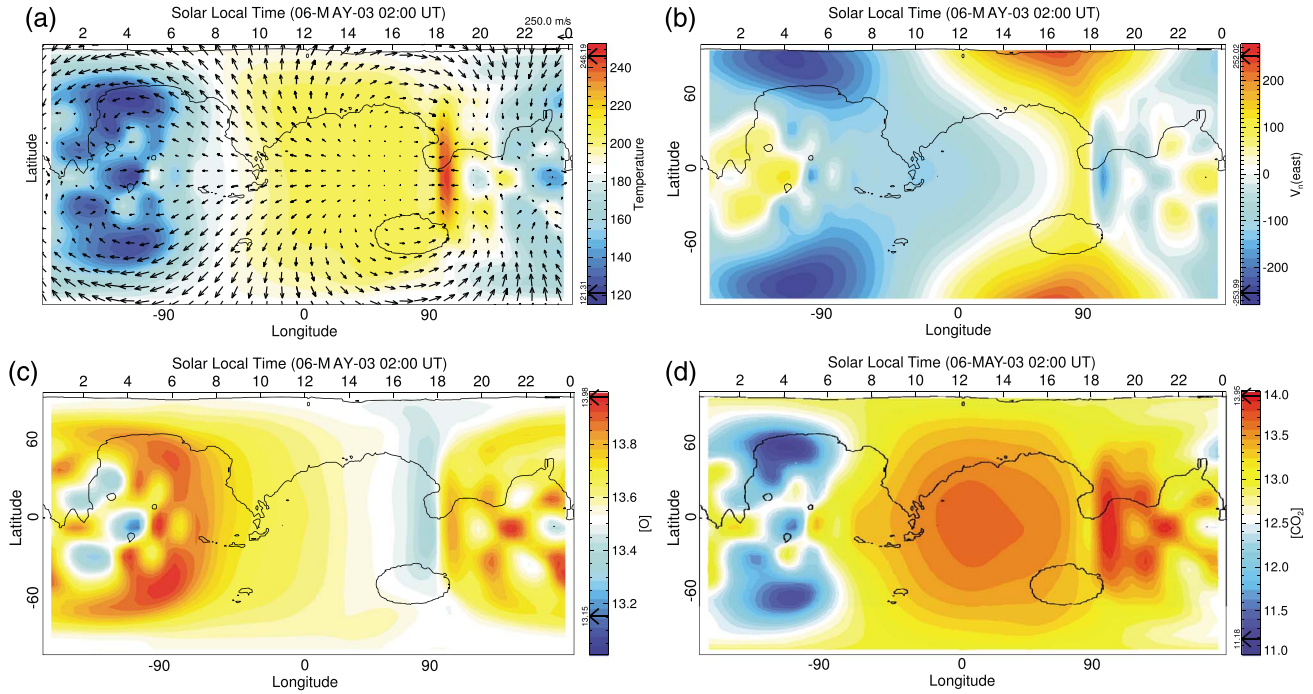

Figure 2. MGITM exobase (~200 km) fields (T, U, O, and CO_2) for equinox/solar minimum conditions. Ls = 180; $F_{10.7}$ = 70; tau = 0.5; CR = 0.003. (a) Temperatures (K), (b) zonal winds (m/s), (c) log10 atomic O densities ($1/m^3$), and (d) log10 CO_2 densities ($1/m^3$). The arrows in Figure 2a indicate the relative magnitude and the direction of the horizontal winds. Zonal wind absolute magnitudes are better displayed in Figure 2b. The color bar in each panel indicates the magnitude of the plotted (color shaded) field.

simulated, and its reasonable match to observations, since the M-GITM upper atmosphere structure and dynamics is built upon this simulated lower atmosphere.

4.1. Upper Atmosphere Solar Cycle Variations at Equinox

Equinox solar minimum and maximum simulations (Ls = 180; $F_{10.7}$ = 70 and 200) are presented first to illustrate the basic features of the simulated Mars upper atmosphere (e.g., the diurnal and spatial variability) and to quantify the solar cycle variations. Figure 2 highlights equinox solar minimum conditions in 2-D slices (latitude versus local time) at ~200 km (temperatures, zonal winds, atomic oxygen densities, and CO_2 densities); Figure 3 presents the same exobase fields on the same 2-D slices for equinox solar maximum conditions.

For solar minimum (SMIN) conditions, solar-driven exobase temperatures (Figure 2a) peak in the midafternoon on the equator (~210 K near LT = 15). Warmer temperatures appear near the evening terminator (LT = 18) but are the result of convergent zonal winds and dynamical heating at this location. Nightside minimum temperatures (~120 K) are visible at approximately LT = 2–4 and at midlatitudes. Diurnal variations are significant (~90 K). Polar temperatures (both North and South) approach ~170–190 K, consistent with strong horizontal winds advecting heat to high latitudes on both the dayside and nightside. Corresponding zonal winds (Figure 2b) reach ~ 250 m/s near the evening terminator (LT = 16–18) and −250 m/s approaching the morning terminator (LT = 4–6). This is consistent with strong meridional winds (not shown) which blow from the equator toward both poles (dayside) and subsequently across the poles onto the nightside, converging on the equator. Vertical winds are descending at this nightside location (LT = 0–4, Latitude (LAT) = 0–30°), resulting in adiabatic heating and the warming of local temperatures. Figure 2d illustrates the CO_2 distribution, which follows closely the diurnal temperature distribution. These CO_2 densities vary by nearly a factor of 600 from day to night at this altitude. Conversely, Figure 2c shows atomic O density distributions that are profoundly different from CO_2; i.e., dayside produced O, from CO_2 photolysis and ion-neutral chemical reactions (see Table 1), is transported to the nightside where bulges are created at low-to-middle latitudes. This transport process, which impacts light species but not CO_2 (i.e., wind-induced diffusion), was illustrated previously in MTGCM simulations [e.g., *Bougher et al.*, 1999b, 2000].

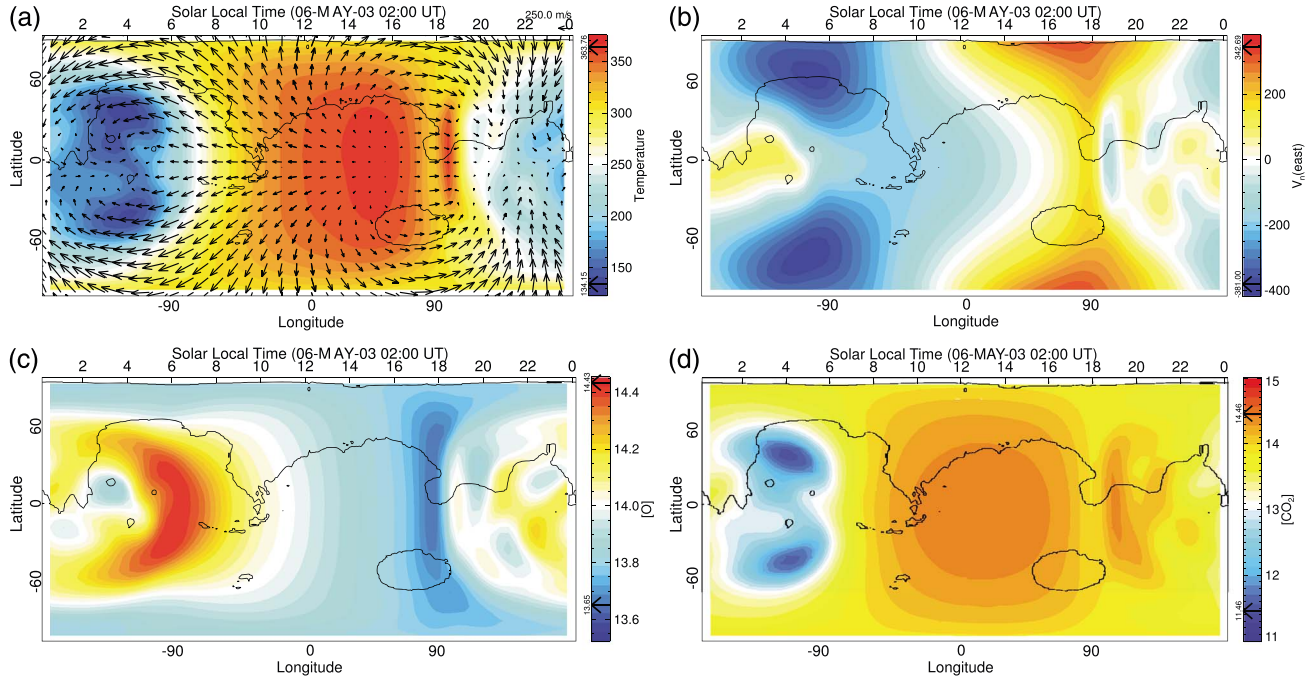

Figure 3. MGITM exobase (~200 km) fields (T, U, O, and CO_2) for equinox/solar maximum conditions. Ls = 180; $F_{10.7}$ = 200; tau = 0.5; CR = 0.003. Same format as Figure 2.

Minimum M-GITM dayside O density values are actually computed on the dayside near the divergence point of the horizonal winds, making day-to-night O density variations as large as a factor of 6.7.

For solar maximum (SMAX) conditions, the same general thermospheric features are reproduced as in Figure 2 for SMIN conditions. However, magnitudes of temperatures, neutral winds, and day-to-night density gradients are generally larger. For instance, simulated exobase temperatures (Figure 3a) continue to peak in the midafternoon on the equator, now reaching ~350 K. Conversely, nightside minimum temperatures approach ~134 K at midlatitudes at approximately LT = 2–5. Diurnal variations of these SMAX temperatures (~215 K) are much larger than for SMIN conditions. SMAX polar temperatures approach ~275–320 K, consistent with stronger (compared to SMIN) horizontal winds (now up to ~350 m/s) advecting heat to high latitudes and onto the nightside. The CO_2 distribution (Figure 3d) now follows the stronger diurnal temperature distribution shown in Figure 3a, yielding a SMAX day-to-night density variation reaching a factor of 950 at this altitude. The atomic O density distribution (Figure 3c) now reveals a day-to-night O density variation as large as a factor of ~6.0. One might expect this day-to-night ratio to be larger for SMAX than SMIN conditions, owing to larger winds advecting O atoms from the dayside to the nightside for the latter. However, the dayside photochemical source of O atoms is also enhanced during SMAX conditions, thus increasing the baseline dayside O densities plus the corresponding reservoir of O atoms available for transport. The net result is a combination of processes that regulate the day-to-night ratio of O atoms at a constant altitude.

Clearly, these M-GITM simulations predict that the solar cycle variation of dayside maximum (215 to 350 K) and nightside minimum (120 to 134 K) temperatures at exobase altitudes (~200 km) gives rise to significant changes in corresponding zonal and meridional winds, as well as diurnal variations in O and CO_2 density distributions. In addition, comparison of the four panels in Figures 2 and 3 suggests that during SMIN conditions, the Mars thermosphere exhibits more wave activity (especially on the nightside) than for SMAX conditions. For example, although not easy to see due to different color scales, SMIN nightside (low-to-middle latitude) temperatures, densities, and winds, all reveal a highly structured pattern that is not reproduced for SMAX simulations at the same location. Such is the case even if common color scales are used. This implies that the Mars lower atmosphere has a stronger effect on upper atmosphere temperature, density, and wind distributions during SMIN conditions, consistent with the Earth. In other words, in situ solar forcing may dominate over wave forcing (of lower atmosphere origin) in the control of Mars

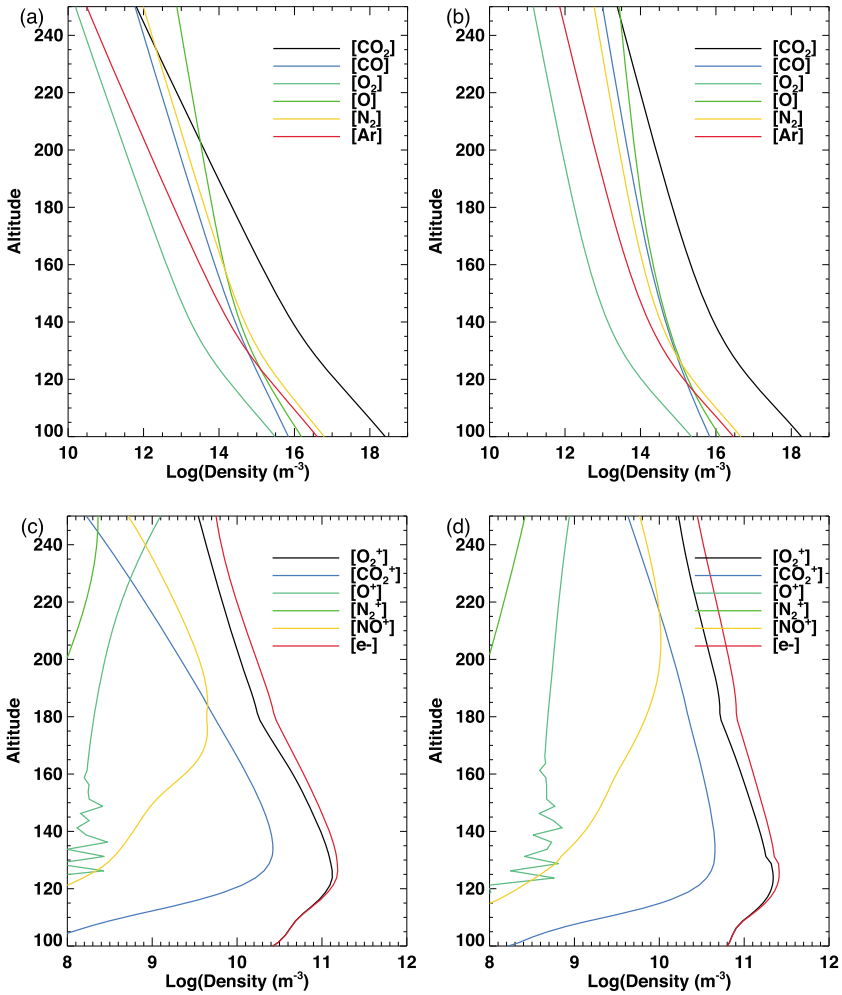

Figure 4. MGITM equinox (solar minimum and maximum) profiles (100–250 km) of (a and b) neutral densities (O, CO, N_2, CO_2, O_2, and Ar) and (c and d) plasma densities (O_2^+, O^+, N_2^+, NO^+, CO_2^+, and e^-) along the equator at LT = 15. O profiles are distinguished from O_2 by the much larger abundances of the former above ~120 km. O^+ profiles are distinguished from N_2^+ by the wiggles below 160 km in the former. Units: log10 densities ($1/m^3$).

thermospheric structure during SMAX conditions. This important characteristic for Mars is partially supported by limited data sets obtained during the Viking Landers 1 and 2 sampling periods during SMIN conditions [e.g., *Seiff and Kirk*, 1977; *Nier and McElroy*, 1977]. Nevertheless, sampling over the entire solar cycle is sparse, and confirmation of this solar cycle effect is still outstanding. Furthermore, for these SMIN and SMAX equinox simulations, it must be emphasized that only solar EUV-UV flux variations, as well as the impacts of migrating solar tides, were included. Other sources of variability such as seasonal forcing, plus upward propagating nonmigrating tides and gravity wave effects, have been neglected thus far.

In order to illustrate and describe altitude variations of temperatures and neutral plus ion densities, profiles are extracted from these same equinox SMIN and SMAX simulations along the equator at LT = 15. This mid afternoon column is chosen to correspond to SZA = 45°, close (but not identical) to Viking 1 sampling conditions, albeit for a different Mars season. Figures 4a and 4b and Figures 4c and 4d contain profiles (100–250 km) of neutral densities and plasma densities for SMIN and SMAX conditions, respectively. Useful metrics that are typically discussed, for comparison of model output to limited observations, include the following: (a) the altitude where the ratio $O/CO_2 = 1.0$, (b) the F_1 peak altitude and magnitude, (c) the O_2^+/CO_2^+ ratio at the F_1 peak, and (d) the O/CO_2 ratio at the same F_1 peak [e.g., *Stewart*, 1987; *Bougher et al.*, 2002, 2014a]. See Table 2.

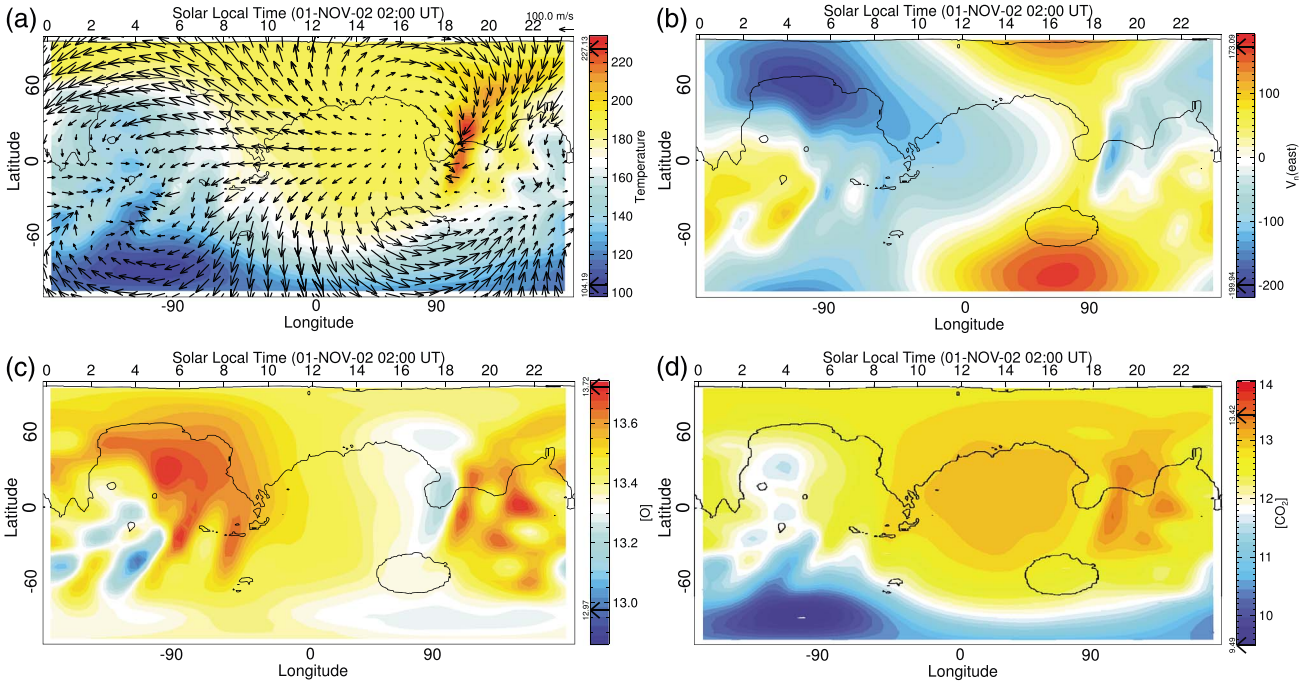

Figure 5. MGITM exobase (~200 km) fields (T, U, O, and CO_2) for aphelion/solar minimum conditions. Ls = 90; $F_{10.7}$ = 70; tau = 0.5; CR = 0.003. Same format as Figure 2.

The M-GITM equinox (Ls = 180) simulations predict that for SMIN conditions, O equals CO_2 near 200 km ($2–3 \times 10^{13}$ m^{-3}) at SZA = 45°, while for SMAX conditions, this ratio equals 1.0 near 240 km (where densities are again both 2 and 3×10^{13} m^{-3}). This rise in the height of the transition from the CO_2 to O dominated regions corresponds to the warmer dayside temperatures (and larger scale heights) for SMAX versus SMIN conditions. Correspondingly, the O mixing ratio at the F_1 peak (~125 km) is ~ 1.8% for SMIN and ~2.5% for SMAX conditions. This means that the dayside SMAX neutral atmosphere is more abundant in atomic O, as expected. This results from the enhanced source of atomic O from CO_2 photolysis (and ion-neutral chemistry) for larger EUV-UV fluxes. This enhanced O abundance is also consistent with an enhanced ionosphere, with larger F_1 peak magnitudes for SMAX (2.51×10^{11}) versus SMIN (1.58×10^{11} m^{-3}) electron densities. In addition, the ratio of O_2^+ to CO_2^+ ions at the F_1 peak is about 4.5 and 5.0 for SMIN and SMAX, respectively. It is noteworthy that small O^+ densities (over 120 to 160 km) are noisy; this is consistent with a known limitation of the chemical solver for low ion densities.

It is also important to notice that the F_1 peak height (~125 km) has not changed between these two cases, again as expected, since the Mars lower atmosphere (below ~115 km) has no response to solar cycle variations in EUV-UV fluxes. Furthermore, this altitude is consistent with the low SZA seasonally averaged F_1 peak height usually quoted from available dayside ionosphere measurements [e.g., *Stewart*, 1987; *Zhang et al.*, 1990; *Withers*, 2009].

4.2. Upper Atmosphere Variations for Solar Cycle and Seasonal Extremes

Calculations have also been performed which examine thermosphere-ionosphere variations under combined solar cycle and seasonal forcing at Mars. Specifically, extreme conditions are examined for which aphelion/solar minimum and perihelion/solar maximum forcing are prescribed. The former corresponds closely to Viking 1–2 descent sampling conditions at Mars in 1976. In addition, MGS (1998–1999) and MRO (2006) aerobraking sampling conditions correspond closely to aphelion/solar minimum-moderate conditions. Perihelion/solar maximum conditions are similar (but not identical) to those experienced by Mariner 6-7 during their flybys in 1969. A detailed description of aphelion/solar minimum plots is given first, with a brief discussion of comparisons with corresponding plots for perihelion/solar maximum conditions.

For aphelion/SMIN conditions, solar-driven exobase temperatures (Figure 5a) peak in the midafternoon at the subsolar latitude (25°N) (~190 K near LT = 15). Temperatures appear warmer near the evening terminator (LT = 18) but again are the result of convergent zonal winds resulting in dynamical heating at this

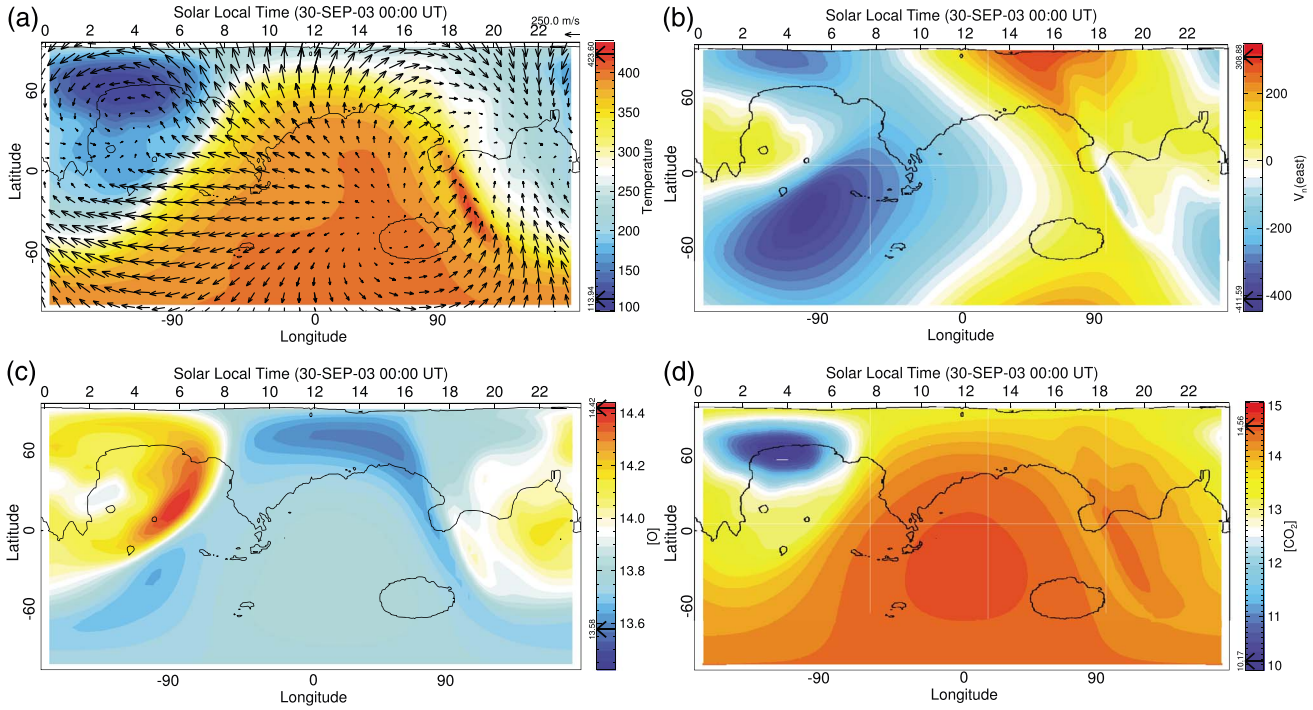

Figure 6. MGITM exobase (~200 km) fields (T, U, O, and CO_2) for perihelion/solar maximum conditions. Ls = 270; $F_{10.7}$ = 200; tau = 0.5; CR = 0.003. Same format as Figure 2.

location. Nightside minimum temperatures (~104 K) are visible at approximately LT = 2–5 and at high southern latitudes, in the polar night. Little dynamical warming is evident in these simulations at these polar night latitudes, yielding cold temperatures (~100 K) at and above 120 km that are consistent with MGS nightside accelerometer mass density measurements and derived temperatures near 120 km (~100–110 K) [*Bougher et al.*, 2006]. Corresponding zonal winds (Figure 5b) are strong in the Southern (winter) Hemisphere, approaching ~ +170 m/s near LT = 16–18, and also in the Northern (summer) Hemisphere approaching −200 m/s near LT = 4–6. This zonal wind asymmetry is consistent with strong meridional winds (not shown) which blow from the subsolar latitude in the Northern (summer) Hemisphere toward both poles and subsequently across the poles onto the nightside, converging on the lower latitudes. This convergence (and the resulting descending winds) again gives rise to adiabatic heating and warming of temperatures just North of the equator near LT = 0–4. The CO_2 distribution (Figure 5d) is asymmetric in latitude, which closely corresponds to the asymmetric diurnal temperature distribution (Figure 2a). These CO_2 densities now vary dramatically from day to night, exceeding a factor of 8000 at this altitude, owing in part to the very cold temperatures in the winter polar night. Conversely, Figure 5c shows atomic O density distributions for which dayside produced O is transported to the nightside by the thermospheric wind system, where it subsequently accumulates at low-to-middle latitudes around LT = 4–8. The maximum day-to-night variation of atomic O approaches a factor of 5.6 (less than simulated for equinox solar minimum or maximum conditions). This is consistent with the fact that aphelion/solar minimum horizontal winds are weakened with respect to either equinox simulation described above, resulting in less efficient day-to-night transport of O atoms.

For perihelion/SMAX conditions (the opposite extreme in solar/seasonal parameters), the same general asymmetric thermospheric features are reproduced as in Figure 5, albeit with the latitudinal sense of the asymmetric distributions reversed. In addition, the magnitudes of SMAX temperatures, neutral winds, and day-to-night density gradients are generally much larger. For example, SMAX mid afternoon exobase temperatures at the subsolar latitude now peak at ~390 K (nearly 200 K warmer than for SMIN). Conversely, SMAX nightside minimum temperatures are only slightly warmer than for SMIN (~114 K) and are now visible at middle-to-high northern (winter) latitudes, once again in the polar night. Little dynamical warming is evident in these SMAX simulations at these polar latitudes (60–90°N), yielding cold temperatures. Such very cold M-GITM temperatures (at and above 120 km) stand in contrast to ODY nightside accelerometer

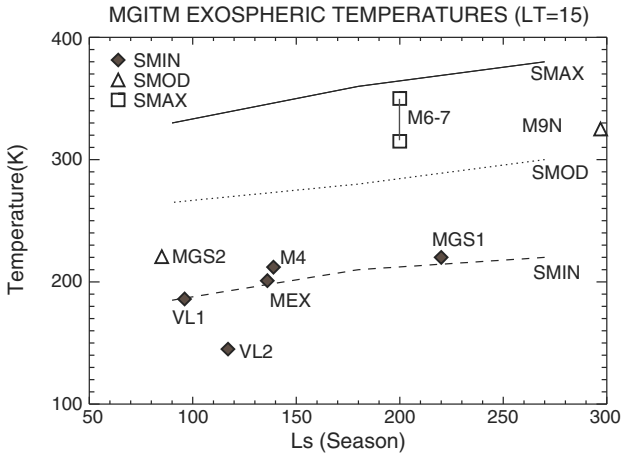

Figure 7. M-GITM dayside (low SZA) exospheric temperatures are plotted against values from previous spacecraft measurements obtained at different Mars seasons and solar cycle conditions [see, e.g., *Bougher et al.*, 2000]. Spacecraft symbols are as follows: diamonds (SMIN conditions, $F_{10.7}$ ~ 70–100), triangles (SMOD conditions, $F_{10.7}$ ~100–130), and squares (SMAX conditions, $F_{10.7}$ ~170–200). Superimposed SMIN (dashed), SMOD (dotted), and SMAX (solid) M-GITM curves illustrate the predicted role of seasonal plus solar cycle forcing. Spacecraft abbreviations plus mean temperatures and 1 σ variability (for multiple measurements) are indicated as follows: VL1 (Viking Lander 1 [186 K]), VL2 (Viking Lander 2 [145 K]), M4 (Mariner [212 ± 17 K]), MEx (Mars Express [201 ± 10 K]), MGS1 (MGS Phase 1 Aerobraking [220 ± 5 K]), MGS2 (MGS Phase 2 Aerobraking [220 ± 6.5 K]), M9N (Mariner 9 nominal mission [325 ± 40 K]), M6-7 (Mariner 6-7 [315–350 ± 75 K]).

measurements (60–90°N) for this season near 120 km (~120–160 K) [*Bougher et al.*, 2006]. Discussion of this discrepancy is given in section 5. Corresponding M-GITM zonal winds (Figure 6b) are strong in the Northern (winter) Hemisphere, approaching ~ +310 m/s near LT = 15–18, and also in the Southern (summer) Hemisphere approaching −410 m/s near LT = 2–6. These SMAX wind magnitudes are about double those simulated for aphelion (SMIN) conditions and appear to be subsonic but close to supersonic values. The CO_2 distribution (Figure 6d) is strongly asymmetric in latitude, which closely corresponds to the asymmetric diurnal temperature distribution (Figure 6a). These CO_2 densities now vary dramatically from day to night, exceeding a factor of 20000 at this altitude. Conversely, the atomic O density distribution (Figure 6c) now reveals a day-to-night O density variation as large as a factor of ~6.92; i.e., significantly greater than that simulated for equinox solar minimum or maximum conditions.

Figure 7 illustrates a composite of M-GITM computed exospheric temperatures in the midafternoon (LT = 15) near the equator (low SZA conditions). Simulated M-GITM temperatures are compared to data extracted values obtained from various spacecraft measurements (see overview discussion in section 2.1). It is clear from this figure that most existing measurements are available for SMIN conditions throughout the Mars seasons. Furthermore, temperatures comprising most of these data sets have been averaged to provide mean values for this plot. The computed M-GITM dayside (low SZA) exospheric temperatures match these SMIN observations reasonably well. In addition, simulated M-GITM temperatures for SMOD conditions (throughout the Mars seasons) are consistent with the limited SMOD measurements. However, the sparse SMAX-measured temperatures (obtained from Mariner 6 to 7) appear to be exceeded by the calculated M-GITM values. In addition, it is noteworthy that the large 1 σ variability of extracted exospheric temperatures from airglow measurements (e.g., Mariner 6-7-9 CO Cameron band emissions and MEx CO_2^+ and CO Cameron band emissions) appears to be uncorrelated with solar activity [e.g., *Stewart*, 1972; *Leblanc et al.*, 2006]. These solar (only) forcing estimates of dayside exospheric temperatures simulated by the M-GITM code are baseline estimates. Further studies are needed to determine the impacts of upward propagating gravity waves and nonmigrating tidal forcing on the variations of computed exospheric temperatures in the M-GITM. See further discussion in section 6.

4.2.1. Solar Minimum Conditions (Ls = 90): VL1 Comparisons

In order to specifically compare existing VL1 measurements with corresponding M-GITM simulated outputs, neutral plus ion density profiles are extracted from SMIN/near aphelion simulations at one location: LT = 16 and LAT = 22.5°N. This column corresponds to SZA = 44°, identical to Viking 1 sampling conditions (Ls = 96, Lat = 22.5°N, LT = 16, $F_{10.7}$ = 69). Figures 8a and 8b contain profiles (100–250 km) of neutral densities (O, CO, N_2, CO_2, O_2, and Ar) and plasma densities (O_2^+, O^+, N_2^+, CO_2+, and e^-) for these SMIN (near aphelion) conditions, respectively.

In Figure 8a, the M-GITM simulated O density equals the CO_2 density near 190 km (~3×10^{13} m^{-3}), while the O mixing ratio at the F_1 peak (~120 km) is ~ 1.8% for these SMIN (aphelion) conditions. The corresponding magnitude of the F_1 peak electron density is ~1.25×10^{11} m^{-3}, which is smaller than calculated for

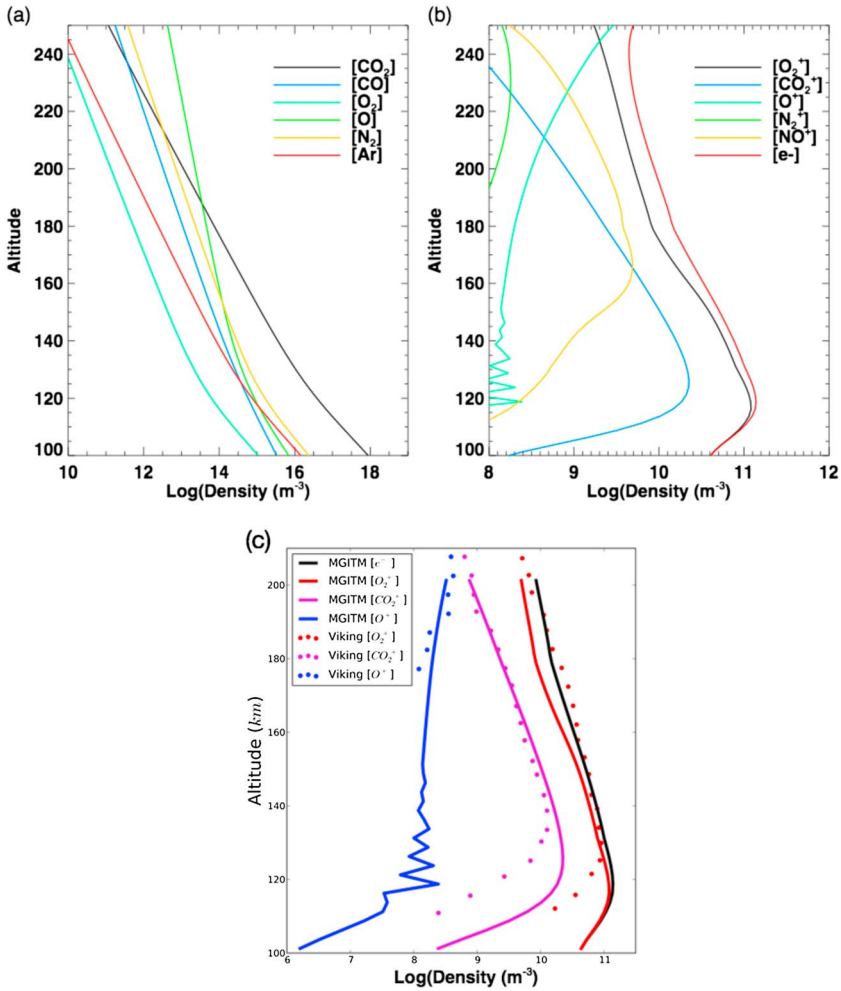

Figure 8. MGITM Aphelion solar minimum profiles (100–250 km) at a single location (LT = 16; LAT = 22.5°N; SZA~ 44°): (a) neutral densities (O, CO, N_2, CO_2, O_2, and Ar); (b) plasma densities (O_2^+, O^+, N_2^+, NO^+, CO_2^+, and Ne); (c) comparison of superimposed (100–200 km) VL1 measured and MGITM simulated plasma densities (O_2^+, O^+, CO_2^+, and Ne). Units: log10 densities ($1/m^3$).

SMIN/equinox conditions (see Figures 8b and 4c). In addition, the ratio of O_2^+ to CO_2^+ ions at the F_1 peak is now ~6.0 for these VL1 conditions.

Each of these standard M-GITM metrics can be compared to VL1 values [*Hanson et al.*, 1977]. For instance, since atomic O was not measured by the Viking UAMS [*Nier and McElroy*, 1977], an O density profile was estimated using a neutral atmosphere model that provided a good match to ion density measurements [*Hanson et al.*, 1977]. For this model, O exceeded CO_2 density near 200 km (~3×10^{13} m^{-3}). Also, the best O mixing ratio at the F_1 peak (i.e., required to provide the measured O_2^+ to CO_2^+ ratio of 8–9 at the same F_1 peak) was determined to be 1.25%.

Figure 8c provides a direct comparison of VL1 measured plasma densities (O_2^+, O^+, CO_2^+, and e^-) with corresponding MGITM profiles at SZA = 44°. The discrepancies between the M-GITM plasma density profiles and those measured by the VL1 RPA instrument are small, but instructive to address. Most importantly, the measured F_1 peak height was determined to occur at ~130 km, which is ~10 km higher than the M-GITM predicts. Both O_2^+ to CO_2^+ simulated ion peaks track lower in altitude than measurements indicate. This discrepancy may indicate that dayside temperatures in the M-GITM middle atmosphere may be slightly cooler than MCS measurements (see section 4.3). Slightly warmer (up to 10 K) middle atmosphere (~60–100 km) temperatures would serve to raise the altitude of the simulated F_1 peak toward the observed value of ~130 km. The computed F_1 peak magnitude (~1.25×10^{11} m^{-3}) is only slighter larger than the value measured (~1.1×10^{11} m^{-3}) by the Viking 1 RPA instrument [*Hanson et al.*, 1977]. Otherwise, a good match

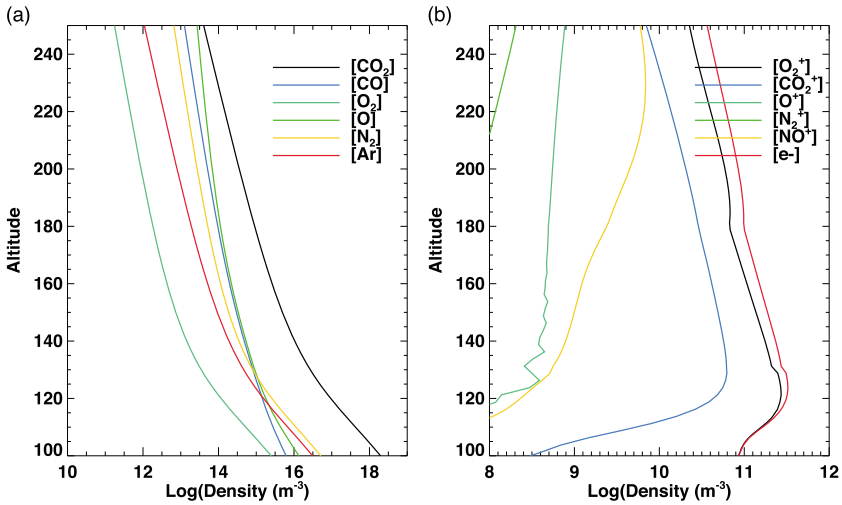

Figure 9. MGITM perihelion solar maximum profiles (100–250 km) of (a) neutral densities (O, CO, N_2, CO_2, O_2, and Ar) and (b) plasma densities (O_2^+, O^+, N_2^+, NO^+, CO_2^+, and Ne) at a single location (LT = 12–15; LAT ~ 10.0S; SZA~ 0–45°). Units: log10 densities ($1/m^3$).

of these data model ion and electron densities is obtained below 200 km, in accord with a photochemical equilibrium dominated lower Martian ionosphere [e.g., *Withers*, 2009; *Haider et al.*, 2011; *Bougher et al.*, 2014a]. It is noteworthy that the measured O_2^+ to CO_2^+ ratio of 8–9 at the 130 km F_1 peak is as much as 50% larger than computed by the M-GITM code at its 120 km F_1 peak. Recall that reaction (R15) (see Table 1) converting CO_2^+ to O_2^+ proceeds rapidly in the presence of atomic O atoms. The computed (smaller) O_2^+ to CO_2^+ ratio suggests an underestimate of the dayside O abundance in the M-GITM code near the ion peak. Enhanced M-GITM dayside O abundances could be achieved by utilizing a smaller value of the peak eddy diffusion coefficient on the dayside, and/or weakening the day-to-night horizontal winds. The latter would reduce the transport of O atoms to the nightside, thereby retaining more O atoms on the dayside near 130 km.

4.2.2. Solar Maximum Conditions (Ls = 270): M67 Comparisons

No spacecraft measurements of neutral and plasma density profiles presently exist for constraining M-GITM simulated profiles for SMAX/near perihelion conditions. Nevertheless, we illustrate these profiles in order to contrast the predicted structure with that displayed above for SMIN/near aphelion conditions. Limited M67 flyby measurements were taken at an average location of LT = 14 near the equator; M-GITM outputs were extracted at this same location as well. This column corresponds to SZA = 30°.

In Figure 9a, the M-GITM simulated O density equals the CO_2 density near 240–250 km (~3×10^{13} m^{-3}), while the O mixing ratio at the F_1 peak (~128 km) is ~ 3.1% for these SMAX/perihelion conditions. The corresponding magnitude of the F_1 peak electron density is ~3.1×10^{11} m^{-3}, which is slightly larger than calculated for SMAX/equinox conditions (compare Figures 9b and 4d). In addition, the ratio of O_2^+ to CO_2^+ at the *F*1 peak is now ~4.0 for these M67 conditions.

These SMAX/near perihelion metrics (approximating M67 conditions) can be compared to corresponding VL1 values for SMIN/aphelion conditions. Clearly, the F_1 peak altitude is higher for M67 (~128 km) than VL1 simulations (~120 km). This is in accord with the expansion of the lower atmosphere during the advance of the Mars seasons [*Withers*, 2009; *Haider et al.*, 2011; *Bougher et al.*, 2014a]. Furthermore, the simulated magnitude of the F_1 peak is larger for M67 (~3.1×10^{11} m^{-3}) than VL1 (~1.25×10^{11} m^{-3}) simulations. This reflects the enhanced SMAX/perihelion versus SMIN/aphelion solar forcing, combining both solar cycle and orbital variations upon the EUV fluxes arriving at Mars. The atomic O abundance at the F_1 peak is computed to grow from 1.8% to 3.1%, which results from the more efficient photolysis of CO_2 producing atomic O during SMAX/perihelion conditions. The latter values are close to those estimated from M67 measurements [*Stewart et al.*, 1972]. Finally, the ratio of O_2^+ to CO_2^+ at the F_1 peak is noted to decrease from 6.0 to 4.0, for VL1 and M67 conditions, respectively. This is contrary to what might be expected with larger O abundances for the latter. However, the larger solar EUV fluxes provide an enhanced initial production of the CO_2^+ ion,

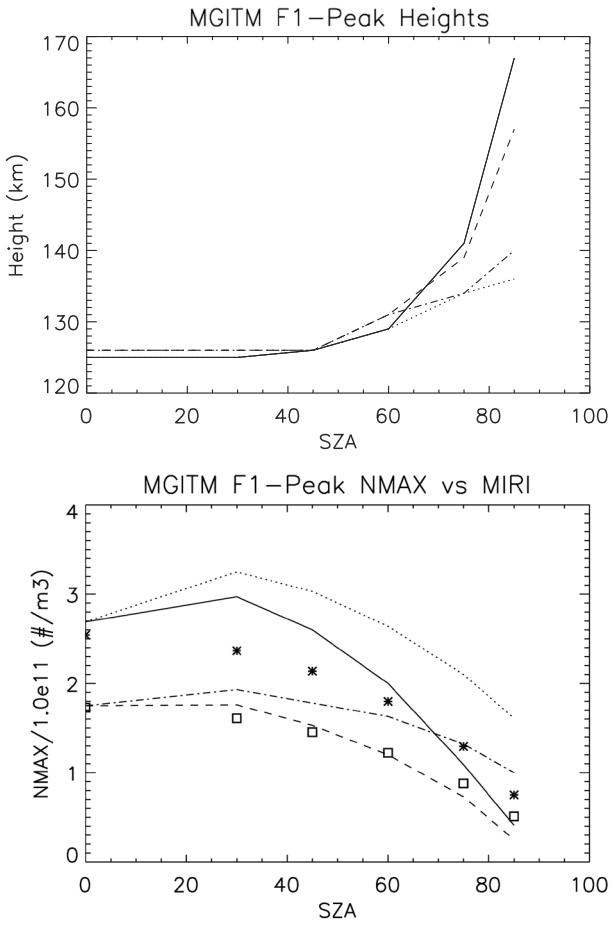

Figure 10. MGITM F_1 peak variations across the dayside: (top) altitudes and (bottom) magnitudes. Dayside (SZA = 0, 30, 45, 60, 75, and 85) values for equinox/equatorial conditions are plotted by four curves: (a) SMAX/afternoon (solid), (b) SMAX/morning (dotted), (c) SMIN/afternoon (dashed), and (d) SMIN/morning (dash dotted). MIRI empirical model values are indicated by asterisks (SMAX) and open squares (SMIN).

prior to the ion-neutral reaction with atomic O yielding O_2^+. Hence, slightly larger O abundances still yield smaller O_2^+ to CO_2^+ ratios for perhelion/SMAX conditions.

4.2.3. Simulated Variations of *F*1 Peak Magnitude and Altitude

Ionospheric F_1 peak magnitude (N_{max}) and height (hmax) variations are a useful diagnostic of the behavior of the photochemical ionosphere within the M-GITM code across its dayside. These variations reflect the following: (a) the changing underlying neutral atmosphere structure (hmax) and (b) the changing solar fluxes received at Mars (N_{max}) (see section 2.2). In particular, the hmax parameter is a great metric to confirm that the Mars lower to upper atmosphere coupling is working properly in the M-GITM code and is realistic throughout the Mars seasons. SZA variations of both of these parameters can be compared in detail with individual pre-MGS, MGS, and MEx data sets. Alternatively, a statistical comparison can be made with corresponding N_{max} variations found in a Mars empirical model of its ionosphere (Mars Initial Reference Ionosphere (MIRI)), currently based upon a huge database of Mars Express MARSIS/Active Ionosphere Sounder (AIS) measurements [e.g., *Mendillo et al.*, 2013].

According to Chapman theory, F_1 peak heights (hmax) should rise with increasing SZA across the dayside, since the altitude where unit optical depth is realized rises as the slant path of the ionizing radiation increases [*Withers*, 2009; *Bougher et al.*, 2014a]. Figure 10a illustrates SZA variations of hmax for both equinox solar maximum (SMAX) and minimum (SMIN) cases. These SZA features are extracted around the equator for afternoon (LT = 12 to 18) and morning (LT = 12 to 6) conditions, in order to investigate if different SZA directions reveal the same hmax and N_{max} behavior. As you move across the afternoon and morningside sectors, the underlying temperature structure is much different; i.e., temperatures are warmer across the afternoon equatorial region approaching the evening terminator (ET), than across the morningside approaching the morning terminator (MT) (see Figures 2a and 3a). Departures of the hmax heights are most noticeable for SZA $\geq 60°$, yielding SZA = 85° ET values (~157–167 km) that are much higher than MT values (136–140 km). Since the height of a given pressure level rises with a warmer (expanded) underlying column, hmax must also rise more rapidly as you approach the ET than the MT, regardless of the slant path conditions. This is precisely what is seen in these M-GITM calculations. This means that hmax at higher SZAs can have different values depending on the underlying neutral atmosphere conditions. This variation of hmax at different locations (e.g., MT versus ET, yet at identical SZAs) provides a useful diagnostic of the underlying neutral atmospheric structure. However, this feature is yet to be confirmed.

Figure 10b illustrates SZA variations of F_1 peak magnitudes (N_{max}) for these same equinox SMAX and SMIN cases, for the same afternoon and morningside conditions. Notice that N_{max} values at the subsolar point differ by a factor of ~1.5, approximately equal to the square root of the change of ion production rates

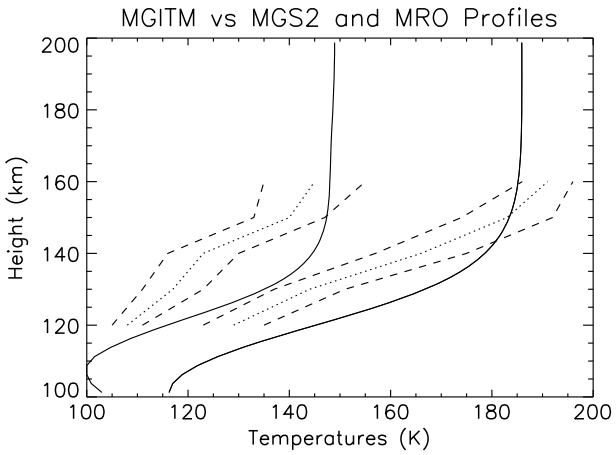

Figure 11. MGITM dayside (LT = 16) and nightside (LT = 3) temperatures profiles (near equator) for near aphelion/solar minimum conditions (solid curves). Superimposed are corresponding MRO (nightside) and MGS (dayside) temperature profiles derived from accelerometer measurements. Dotted curves correspond to the averaged dayside and nightside derived temperature profiles. Dashed curves illustrate the 1 sigma error bars corresponding to these mean values. Simulated exospheric temperatures are ~186 K (dayside) and ~150 K (nightside). See *Keating et al.* [2008] and *Bougher et al.* [2014a].

between these two cases. The absolute values for SMAX ($\sim 2.7 \times 10^{11}$ m^{-3}) and SMIN ($\sim 1.75 \times 10^{11}$ m^{-3}) compare favorably with those gleaned from previous models and data sets [e.g., *Zhang et al.*, 1990; *Withers*, 2009], and also with MIRI empirical model values at the subsolar point [*Mendillo et al.*, 2013]. N_{max} values decrease toward the terminator, as Chapman theory would predict. However, the rate of this decrease toward SZA = 85° is faster in the afternoon sector than in the morningside sector. Attenuation of the solar ionizing radiation is larger in the afternoon sector for SZA $\geq$ 40°; this occurs because of the expanded neutral atmospheric column due to the warmer (underlying) temperatures. This results in reduced afternoon N_{max} values compared to those calculated for the morningside sector; i.e., these afternoon N_{max} SZA variations are generally consistent with MIRI empirical model behavior. This variation of N_{max} at different locations (e.g., MT versus ET, yet at identical SZAs) also needs to be explicitly confirmed. However, estimation of the total electron content and its variations with SZA (MT versus ET) does indeed show higher N_{max} values in the morningside than in the eveningside [*Safaeinili et al.*, 2007]

4.2.4. Diurnal Variations at Aphelion/SMIN Conditions

Figure 11 compares MGS and MRO aerobraking derived temperature profiles near the equator (for LT = 16 and 3) with corresponding temperature profiles extracted from the M-GITM solar minimum (aphelion) case (i.e., also used for VL1 studies above). It is remarkable that the aphelion season thermospheric structure is quite repeatable for these two Martian years [*Keating et al.*, 2008; *Bougher et al.*, 2014a]. Topside (above 160 km) temperatures are computed to range from 186 K (dayside) to 145 K (nightside), in reasonable agreement with aerobraking derived values [e.g., *Keating et al.*, 2008; *Bougher et al.*, 2014a]. However, at lower altitudes (~120–150 km), M-GITM simulated temperatures are ~0–23 K (dayside) and ~5–20 K (nightside) warmer than measured (mean) temperatures suggest. This mismatch of lower thermosphere data and model temperatures may be partially due to the improper placement of the mesopause altitude in the current M-GITM calculations; i.e., raising the simulated mesopause altitude by ~10 km would improve the comparison, especially on the dayside. However, nightside mesopause temperatures (~105 K) and heights (~103 km) from SPICAM stellar occultation measurements are consistent with M-GITM temperatures [*Forget et al.*, 2009; *McDunn et al.*, 2010]. This implies that a reexamination of dayside and nightside thermospheric IR cooling is needed for these aphelion model simulations. Discussion of this potential cooling is found in section 5.

The diurnal variation of thermospheric mass densities can also be extracted from these same aphelion aerobraking measurements. Figure 14.5 from *Bougher et al.* [2014a] illustrates measured equatorial mass densities at 130 km that vary from ~1.6 kg/km^3 (LT = 16) to ~0.22 kg/km^3 (LT = 3), yielding a diurnal variation of a factor of ~7.0. By contrast, corresponding M-GITM mass densities (at the same locations) vary from ~1.0 kg/km^3 (LT = 16) to ~0.5 kg/km^3 (LT = 3), yielding a diurnal variation of a factor of ~2.0. This discrepancy is largely connected to the warmer 130 km temperatures computed by the M-GITM on the nightside at this altitude (see Figure 11) compared to those observed. Further discussion will be provided in section 5.

4.3. Lower to Middle Atmosphere Variations for Seasonal Conditions

Figure 12 illustrates M-GITM meridional cross sections (latitude versus altitude) of lower atmosphere (~0–90 km) temperatures for three seasons (Ls = 90, 180, and 270) at LT = 15. These 2-D plots are compared

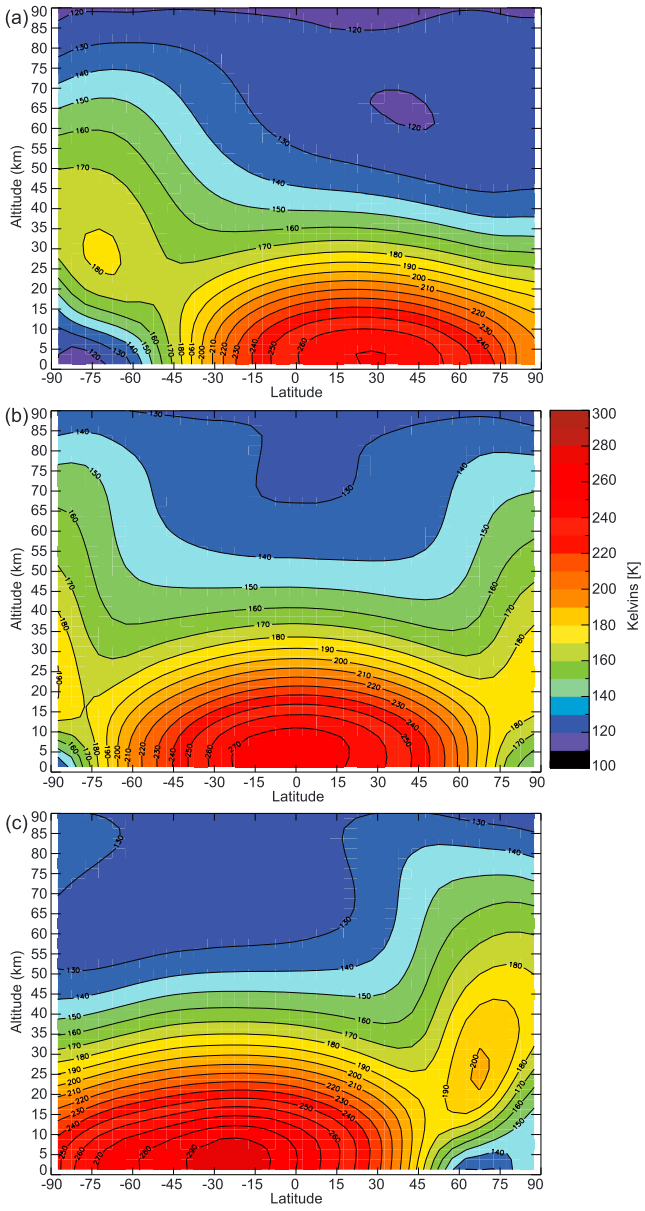

Figure 12. MGITM temperature cross sections (0–90 km) for three seasons and dayside conditions (LT = 15): (a) Ls = 90, (b) Ls = 180, and (c) Ls = 270. Each of these three panels presents an altitude (0–90 km) versus latitude map of temperatures for annual- (and global-) averaged dust conditions (tau = 0.5, CR = 0.003). Comparisons are made with corresponding MRO/MCS temperature slices given in Figure 13. Both Figures 12 and 13 have the same color scale (and color bar) to aid in the comparison of the two.

to corresponding MRO/MCS temperature cross sections for MY30, shown in Figure 13. Diurnal surface temperatures in M-GITM are parameterized to closely match empirical values; dayside surface temperatures range from ~274 K (aphelion) to 300 K (perihelion) at the subsolar latitude for these seasons.

A comparison of M-GITM and MCS lower-middle atmosphere temperatures for these three seasonal slices shows regions of discrepancy that are important to discuss. Above ~50 km, M-GITM middle atmosphere temperatures are simulated to be as much as 10–20 K cooler than MCS observations indicate. This situation is clearly evident for aphelion conditions, where cooler middle atmosphere temperatures are consistent with simulated dayside *F*1 peak heights that are ~8–10 km lower than Viking Lander 1 observations indicate (see section 4.2.1). Future planned improvements in the non-LTE CO_2 15 μm cooling routine (as well as the parameterized altitude transition from LTE to non-LTE conditions) will be implemented to address this problem. In addition, near surface temperatures (~0–30 km) are calculated to be as much as 40–50 K warmer than MCS observations, especially near 30 km. It is notable that M-GITM near IR heating and CO_2 15 μm cooling rates at these altitudes compare well (both magnitude and altitude location) with corresponding NASA AMES MGCM model heating and cooling rates for these same seasonal slices [*Mischna et al.*, 2012]. This suggests missing lower atmosphere physics in the M-GITM code, including (a) a planetary boundary layer (PBL) scheme with corresponding convection and its vertical redistribution of thermal energy and (b) Martian topography. The incorporation of the former will indeed cool the lower atmospheric bottom-scale height temperatures in M-GITM toward empirical values; incorporation of the latter will also modify near surface temperatures. The question remains, will these near surface atmosphere improvements to M-GITM (below 50 km) modify its upper atmosphere structure and dynamics? Recent comparisons of a 1-D Mars radiative-convective model [*Vasavada et al.*, 2012; *Haberle et al.*, 1999] and the corresponding 1-D application of M-GITM suggest that (a) the incorporation of a PBL scheme in M-GITM will not likely impact its upper atmosphere and (b) the application of eddy thermal conductivity below 50 km will not impact upper atmosphere temperatures. However, the incorporation of topography will impact upper atmosphere structure and dynamics, as indicated previously *Bell et al.* [2007].

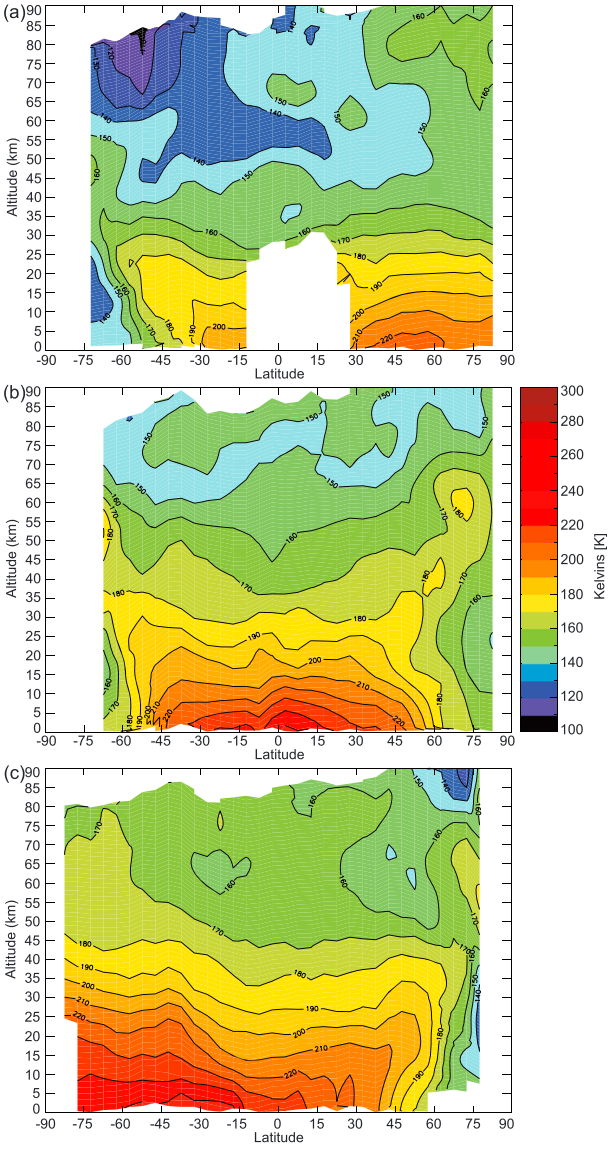

Figure 13. MRO/MCS temperature cross sections (0–90 km) for three seasons and dayside (LT = 15) conditions: (a) Ls = 90, (b) Ls = 180, and (c) Ls = 270. Each of these three panels presents an altitude versus latitude map of temperatures for MY30 for which seasonal dust evolution was nominal (no large dust events, rather weak dusty season).

In short, a combination of gradual improvements to M-GITM lower atmosphere physics will indeed enable 0–30 km temperatures to much better approximate observed values (as indicated by MY30 MCS v4.0 data sets) without adversely impacting its upper atmosphere structure. See sections 5 and 6 for more details.

Observed polar warming features in the Martian lower atmosphere are another important check on the capability of the M-GITM code to reproduce actual MY30 temperature distributions. For equinox conditions, in each hemisphere, temperatures decrease toward the poles below ~15–20 km. Minimum surface temperatures reach ~115–140 K at the poles (near the surface). Above ~ 35–40 km (extending to at least ~ 80 km), there is a temperature minimum at the equator and a temperature maximum at middle to high latitudes in each hemisphere. These maxima migrate closer to the poles with increasing altitude (up to ~ 35–40 km or so) and appear very near the poles at higher altitudes. The equatorial temperatures at/above ~60 km are quite cold (~125–130 K), while polar temperatures at these altitudes vary from 170 to 140 K (from 60 to 80 km). These polar warming features (above ~20 km) are indicative of a two-cell circulation, where a Hadley cell forms in each hemisphere providing dynamical heating at middle to high latitudes [e.g., *McCleese*, 2008; *McDunn et al.*, 2013]. However, the reduced magnitude of the polar warming (compared to MCS observations) and its initial onset at lower altitudes both suggest that the M-GITM simulated meridional circulation is too weak.

For aphelion (solstice) conditions, in the winter hemisphere, temperatures decrease toward the South Pole below ~20 km, yielding minimum surface temperatures of ~110 K at the winter pole. Above ~30–35 km (extending to at least ~ 70 km), there is a temperature minimum at the Northern low-to-middle latitudes and a temperature maximum at middle to high latitudes in the winter hemisphere. These maxima migrate closer to the poles with increasing altitude (extending up to ~40–45 km or so) and appear very near the poles at higher altitudes. The magnitudes of these polar maxima range from 180–185 K (~25–40 km) to 125–135 K (~70 km). Conversely, the Northern midlatitude temperatures spanning ~40 to 70 km are quite cold (~145–150 to 115 K). These polar warming features in the Southern Hemisphere (above ~20 km) are indicative of a single cell circulation, where a Hadley cell forms with rising motion in the summer hemisphere (Northern latitudes) and descending motion in the winter hemisphere (Southern latitudes), providing dynamical heating at middle to high latitudes approaching the South Pole [e.g., *McCleese*, 2008; *McDunn et al.*, 2013]. By comparison, the magnitudes of the MCS polar warming

temperature maxima (~160–170 K at 40–50 km, and ~120–130 K at 70 km) are not quite as large as those simulated by M-GITM. However, the initial onset of observed winter polar warming at ~30–35 km is similar to that simulated.

For perihelion (solstice) conditions, in the winter hemisphere, temperatures decrease toward the North Pole below ~20 km, yielding minimum surface temperatures of ~120 K at the winter pole. Above ~30–35 km (extending to at least ~ 70 km), there is a temperature minimum at the Southern low-to-middle latitudes and a temperature maximum at middle to high latitudes in the winter hemisphere. These Northern Hemisphere maxima migrate closer to the poles with increasing altitude (extending up to ~60 km or so) and appear to recede from the pole at higher altitudes. The magnitudes of these polar maxima range from 195–205 K (~25–30 km) to 145–155 K (~70 km). Conversely, the Southern midlatitude temperatures spanning ~30 to 70 km are colder (~180–190 to 112–120 K). These polar warming features (above ~30 km) are again indicative of a Hadley cell which forms with rising motion now in the summer hemisphere (Southern latitudes) and descending motion in the winter hemisphere (Northern latitudes), providing dynamical heating (cooling) at middle to high latitudes approaching the North Pole (at low-to-middle latitudes in the summer hemisphere). By comparison, the magnitude of the corresponding MCS polar warming temperature maximum (~180–190 K at 50–60 km) is not quite as warm as that simulated by M-GITM (~200 K). In addition, this altitude of observed peak temperatures is nearly 25–30 km higher than simulated.

Clearly (and especially for perihelion conditions), this suggests that missing physical processes are at work in the real Mars atmosphere that the M-GITM code is not presently capturing. For instance, more appropriate horizontal and vertical dust distributions need to be specified in the M-GITM code consistent with representative perihelion conditions (i.e., a globally uniform, constant dust opacity is not sufficient). This will modify the aerosol heating that helps drive the circulation. Furthermore, the M-GITM simulated (lower atmosphere) circulation requires fine tuning throughout the Mars seasons with the application of a gravity wave momentum deposition scheme. Such numerical schemes could provide enhanced meridional flows in response to retarded zonal winds in the middle atmosphere. Subsequently, a more realistic lower atmosphere temperature structure may result, consistent with observed polar warming features during MY30 [*McCleese*, 2008; *McDunn et al.*, 2013].

5. Discussion and Implications

Periodic solar forcing (e.g., over both solar cycle and solar rotation timescales) has the potential to significantly regulate the Martian upper atmosphere temperature, composition and global wind structure. This is clearly evident in the M-GITM equinox solar maximum (SMAX) and solar minimum (SMIN) simulations. For instance, conducted M-GITM simulations predict that the solar cycle variation of dayside maximum (215 to 350 K) and nightside minimum (120 to 134 K) temperatures at exobase altitudes (~200 km) gives rise to large changes in corresponding zonal and meridional winds (i.e., ~100 m/s variation), as well as O (nightside bulge) and CO_2 (dayside maximum) density distributions. Global patterns of the wind system are shown to persist with the advance of the solar cycle, but the changing magnitudes of the winds are directly connected to the underlying pressure (density and temperature) gradients that are strongly varying. Limited spacecraft measurements have been obtained thus far near equinox conditions to constrain these specific M-GITM predictions over the solar cycle.

However, available data sets do suggest that other nonsolar forcing agents may be important in regulating upper atmosphere structure as well. For instance, dayside exospheric temperatures have been carefully estimated from airglow emissions using MEx/SPICAM data sets [e.g., *Leblanc et al.*, 2006; *Stiepen et al.*, 2014]. Most of these available MEx data sets have been obtained during SMIN to SMOD conditions. Nevertheless, the correlation of the observed dayside exospheric temperature variations with respect to SZA (or the changing solar fluxes received at the planet) is small. This implies that nonsolar forcing is also important and may modulate or overwhelm the periodic solar forcing under certain conditions [e.g., *Stewart*, 1972]. This nonsolar forcing may be attributed to the impacts of upward propagating nonmigrating tides and gravity waves [*Stewart et al.*, 1972; *Bell et al.*, 2007; *Bougher et al.*, 2009; *González-Galindo et al.*, 2009b; *Medvedev et al.*, 2011; *Medvedev and Yiğit*, 2012; *Stiepen et al.*, 2014]. Hence, the M-GITM solar cycle variations presented in this paper should be used as baseline estimates. Further investigations focused upon the

impacts of these upward propagating wave effects will use these M-GITM predictions as a starting point for comparative studies.

The large Mars orbital eccentricity demands that both the solar cycle and seasonal variations in the solar forcing (impacting the upper atmosphere structure and winds) should be considered together [e.g., *Bougher et al.*, 2000]. This is clearly demonstrated when comparing the M-GITM equinox and "extreme" solar cycle cases described in sections 4.1 and 4.2. For instance, mid afternoon equatorial temperatures near ~200 km are predicted to vary from ~210 to 350 K (equinox) and ~190 to 390 K (aphelion to perihelion) over the solar cycle. The pressure gradients resulting from these temperature (and underlying density) variations drive zonal and meridional winds that vary by a factor of 2 (~200 to 400 m/s) over these same extreme conditions, while equinox variations are smaller (~250 to 350 m/s). Diurnal variations of atomic O and CO_2 are generally anticorrelated for both equinox and extreme cases, with O atoms being transported from their dayside source to the nightside where bulges are produced. However, the nightside buildup of atomic O is largest for SMAX/perihelion case, which is consistent with the strongest day-to-night thermospheric winds for these conditions.

The best constraints that presently exist for the Mars thermosphere-ionosphere structure were obtained for SMIN/aphelion conditions, enabling M-GITM simulations to be directly compared with Viking Lander 1 neutral and ion density and temperature measurements (see section 4.2.1). Single location (SZA ~ 44°) neutral and ion profile data model comparisons are quite good, suggesting that the M-GITM simulated structure spanning ~100 to 200 km is generally realistic for this set of input conditions. Horizontal variations of temperatures for this same SMIN/aphelion case can be compared with MGS aerobraking data [*Bougher et al.*, 2006]. Simulated warm dayside thermospheric temperatures are shown to give way to very cold temperatures (~104 K) in the winter polar night (at/above ~120 km), in accord with MGS measurements. This confirms that dynamical heating from the interhemispheric thermospheric circulation should be minimal during the aphelion season, as previously shown with MTGCM simulations [e.g., *Bougher et al.*, 2006].

Conversely, little SMAX data are available for comparison with SMAX/near perihelion simulations (see section 4.2.2). Nevertheless, limited ODY SMAX aerobraking measurements were used to extract a strong winter polar warming feature in the Northern Hemisphere (60–90°N) for this season near 120 km (temperatures of ~ 120–160 K). Simulated M-GITM temperatures at this altitude for the winter polar night are much colder (~115–120 km), implying that M-GITM does not capture the full dynamical heating that is required from the interhemispheric circulation. This discrepancy points to two missing physical parameterizations that are not accounted for in these simulations: (a) upward propagating tidal (nonmigrating) forcing resulting from surface topography and (b) gravity wave momentum deposition and the impacts on the global winds and corresponding temperature structure. Topographic forcing has been neglected thus far (i.e., coded yet turned off, see section 6) in these M-GITM simulations in order to provide a baseline against which new topographically forced simulations can be compared. It is anticipated that stronger meridional winds and warmer polar night temperatures will be realized with this included tidal forcing, as previously demonstrated by various Mars upper atmosphere models [e.g., *Bougher et al.*, 2006; *Bell et al.*, 2007; *González-Galindo et al.*, 2009b]. In addition, it is expected that simulated low SZA temperatures will be cooler owing to enhanced upwelling winds on the dayside [*Bougher et al.*, 2000]. Furthermore, the impacts of gravity wave momentum deposition can be investigated, for both the Mars coupled lower and upper atmospheres, with the incorporation of a suitable gravity wave scheme that captures both lower and upper atmosphere dissipation mechanisms. The parameterization scheme of *Medvedev et al.* [2013] will be used, since it allows for the effects of waves with both zero and nonzero phase speeds to be accommodated (the latter dominate in the middle and upper atmosphere). In addition, the Palmer-type scheme mentioned in section 3.5.3 will be used to address zero-phase speed (orographic-induced) wave effects only.

In situ sampling able to investigate the diurnal variation of the Martian thermosphere is presently limited to aerobraking measurements (see sections 2.1 and 4.2.4). Accelerometer mass densities have been used to derive neutral temperatures for constraining models. For example, comparison of M-GITM simulated dayside and nightside (equatorial) temperature profiles (~100–160 km) with corresponding MGS and MRO derived temperatures (section 4.2.4) reveals that simulated temperatures are generally warmer (by as much as ~20 K) in both the dayside and nightside lower thermosphere. The incorporation of Martian topography, and the associated nonmigrating tidal impacts on the thermospheric circulation, has been shown to provide dayside cooling and polar night warming in thermospheric global models [e.g., *Bell et al.*, 2007;

González-Galindo et al., 2009b]. Hence, further progress in the investigation of diurnal variations will require that Mars topography be turned on in M-GITM. In addition, calculation of improved temperature structure near the Mars mesopause will likely require an improved CO_2 15 μm cooling scheme, as implemented recently in *González-Galindo et al.* [2013].

6. Future Features

The primary goal of developing M-GITM is to be able to accurately characterize the state of the Mars upper atmosphere for a variety of planetary and heliospheric conditions. In order to accomplish this goal, it is necessary to include the Martian lower and middle atmosphere within the model domain (0–250 km), as well as some of the dominant physical processes that shape this region of the atmosphere (see section 3.5). Nevertheless, we elected to assume that some middle and lower atmospheric processes, such as CO_2 condensation and sublimation plus planetary boundary layer physics, have a negligible impact on the state of the upper atmosphere at this stage of the model development (i.e., focusing instead on the more relevant processes impacting the upper atmosphere). These neglected middle-lower atmosphere processes, and their effects on the thermal and dynamical coupling linking the Martian lower and upper atmospheres, will be investigated in future updates of the M-GITM code.

In addition, the results discussed in this paper also neglect the effects of several important processes known to significantly impact the upper atmosphere. In particular, the effects of topography are not included at this point. M-GITM has been adapted to use a terrain following vertical coordinate system by modifying the vertical solver and vertical boundary conditions, while making use of the topography measurements provided by the Mars Orbiter Laser Altimeter (MOLA) instrument onboard MGS [*Smith and Zuber*, 1996]. The formulation of the altitude vertical coordinate system follows that outlined in [*Kasahara*, 1974]. Work is currently underway to quantitatively evaluate the effects of topography on the global Mars upper atmosphere. Due to the detailed nature of this study, the results are excluded from this paper and will be submitted for publication in upcoming papers.

Additionally, the 60 moment spherical harmonic expansion of Mars' crustal fields developed by *Arkani-Hamed* [2002] has been implemented into the M-GITM code. In the presence of a magnetic field, M-GITM inherits its ion advection solver from the terrestrial version of GITM [*Ridley et al.*, 2006]. Again, a detailed quantification of the effects of the crustal magnetic fields is underway and results from that study will be published in the near future.

Finally, work is presently being done to integrate the M-GITM code with the Michigan MHD (magnetohydrodynamic, plasma) and the AMPS (Adaptive Mesh Particle Simulator, exosphere) codes for the self-consistent simulation of the Mars thermosphere-ionosphere-exosphere regions and the solar wind interaction with the planet. This model integration activity will make use of the existing Michigan Space Weather Modeling Framework (SWMF). The SWMF is a fully functional and high-performance computational framework developed to enable the integration of a number of numerical models of the entire Sun-heliosphere-Earth system for space weather modeling [*Tóth et al.*, 2005]. Application to Mars will enable these three independent models to exchange fields with one another (two-way coupling). The ultimate goal is to self-consistently address volatile escape processes and the corresponding loss rates from modern Mars for comparison with anticipated MAVEN neutral and plasma data sets that are forthcoming starting in 2014.

7. Conclusions

This paper summarizes the main features of a new nonhydrostatic global circulation model of the Mars atmosphere, M-GITM, that focuses on solving for the state of the thermosphere and ionosphere system. M-GITM is based on the terrestrial GITM model [*Ridley et al.*, 2006] and makes use of Mars specific parameters and physical processes from several existing Mars codes, including the Mars thermosphere general circulation model (MTGCM) and the NASA Ames Mars GCM. M-GITM self-consistently solves for the neutral densities, winds, and temperatures as well as the ion and electron densities, and the neutral winds while assuming a photochemical ionosphere. We compare the model against a wide range of neutral and ion measurements across a variety of local times, solar zenith angles plus solar cycle, and seasonal conditions.

M-GITM reproduces the measured temperature and density structure of the upper atmosphere reasonably well, though the comparisons depend highly on the conditions. The best data model comparisons thus far

are focused upon aphelion (solar minimum) conditions, closely approximating the sampling environment during the Viking Landers 1 and 2 descents. For instance, low SZA exospheric temperatures near ~200 km are predicted to be 190 K, in accord with Viking 1 values. Simulated neutral densities reveal that O exceeds CO_2 at about 190 km, with a corresponding O/CO_2 mixing ratio of 1.8% at 120 km. Finally, the calculated F_1 peak electron density is $\sim 1.25 \times 10^{11}$ m^{-3} at 120 km, in accord with measured Viking RPA densities. Overall, the present M-GITM code is a production level research tool of the Mars thermosphere-ionosphere system that has many potential applications for future Mars studies.

Acknowledgments
Funding support for this work was provided in part by the National Science Foundation (NSF) through grant ATM-0535811 to the University of Michigan. In addition, the Mars Data Analysis Program (MDAP) also supported a portion of this research through NASA grant NNX10AO17G. Finally, the authors wish to acknowledge extensive use of NAS supercomputer facilities in the production of the M-GITM simulations presented in this paper. All Mars data sets used to validate the M-GITM model can be accessed via the NASA PDS or the ESA PSA. All outputs required to create the M-GITM figures and tables in this paper can be accessed via data cubes to be supplied by the corresponding author upon request. Contact email: bougher@umich.edu.

References

Angelats i Coll, M., F. Forget, M. A. López-Valverde, and F. González-Galindo (2005), The first Mars thermospheric general circulation model: The Martian atmosphere from the ground to 240 km, *Geophys. Res. Lett.*, *32*, L04201, doi:10.1029/2004GL021368.

Arkani-Hamed, J. (2002), An improved 50-degree spherical harmonic model of the magnetic field of Mars derived from both high-altitude and low-altitude data, *J. Geophys. Res.*, *107*(E10), 5083, doi:10.1029/2001JE001835.

Baird, D. T., R. Tolson, S. Bougher, and B. Steers (2007), Zonal wind calculations from Mars global surveyor accelerometer and rate data, *J. Spacecraft Rockets*, *44*, 1180–1187, doi:10.2514/1.28588.

Banks, P. M., and G. Kockarts (1973), *Aeronomy*, vol. 1, Aerospace, U. K.

Baumgaertner, A. J., R. Neely III, G. Lucas, and J. Thayer (2013), Towards a comprehensive global electric circuit model: Conductivity and its variability in WACCM model simulations, in *EGU General Assembly Conference Abstracts*, vol. 15, pp. 6670, Copernicus Meetings, Gottingen, Germany.

Bell, J. M., S. W. Bougher, and J. R. Murphy (2007), Vertical dust mixing and the interannual variations in the Mars thermosphere, *J. Geophys. Res.*, *112*, E12002, doi:10.1029/2006JE002856.

Bell, J. M., J. Westlake, and J. H. Waite, Jr. (2011a), Simulating the time-dependent response of Titan's upper atmosphere to periods of magnetospheric forcing, *Geophys. Res. Lett.*, *38*, L06202, doi:10.1029/2010GL046420.

Bell, J. M., J. H. Waite, Jr., J. Westlake, S. W. Bougher, A. J. Ridley, R. Perryman, and K. E. Mandt (2014), Developing a self-consistent description of Titan's upper atmosphere without hydrodynamic escape, *J. Geophys. Res. Space Physics*, *119*, 4957–4972, doi:10.1002/2014JA019781.

Bell, J. M., et al. (2011b), Simulating the one-dimensional structure of Titan's upper atmosphere: 3. Mechanisms determining methane escape, *J. Geophys. Res.*, *116*, E11002, doi:10.1029/2010JE003639.

Bougher, S., and D. Huestis (2010), Solar cycle variation of Mars exospheric temperatures: Critical review of available dayside measurements and recent model simulations, in *38th COSPAR Scientific Assembly*, vol. 38, pp. 1410, Copernicus Meetings, Gottingen, Germany.

Bougher, S., G. Keating, R. Zurek, J. Murphy, R. Haberle, J. Hollingsworth, and R. T. Clancy (1999a), Mars global surveyor aerobraking: Atmospheric trends and model interpretation, *Adv. Space Res.*, *23*, 1887–1897, doi:10.1016/S0273-1177(99)00272-0.

Bougher, S. W., S. Engel, R. G. Roble, and B. Foster (1999b), Comparative terrestrial planet thermospheres: 2. Solar cycle variation of global structure and winds at equinox, *J. Geophys. Res.*, *104*, 16,591–16,611, doi:10.1029/1998JE001019.

Bougher, S. W., S. Engel, R. G. Roble, and B. Foster (2000), Comparative terrestrial planet thermospheres: 3. Solar cycle variation of global structure and winds at solstices, *J. Geophys. Res.*, *105*, 17,669–17,692, doi:10.1029/1999JE001232.

Bougher, S. W., R. G. Roble, and T. Fuller-Rowell (2002), Simulations of the upper atmospheres of the terrestrial planets, *Geophys. Monogr. Ser.*, *130*, 261–288.

Bougher, S. W., S. Engel, D. Hinson, and J. Murphy (2004), MGS radio science electron density profiles: Interannual variability and implications for the Martian neutral atmosphere, *J. Geophys. Res.*, *109*, E03010, doi:10.1029/2003JE002154.

Bougher, S. W., J. M. Bell, J. R. Murphy, M. A. Lopez-Valverde, and P. G. Withers (2006), Polar warming in the Mars thermosphere: Seasonal variations owing to changing insolation and dust distributions, *Geophys. Res. Lett.*, *33*, L02203, doi:10.1029/2005GL024059.

Bougher, S. W., P.-L. Blelly, M. Combi, J. L. Fox, I. Mueller-Wodarg, A. Ridley, and R. G. Roble (2008), Neutral upper atmosphere and ionosphere modeling, *Space Sci. Rev.*, *139*, 107–141, doi:10.1007/s11214-008-9401-9.

Bougher, S. W., T. M. McDunn, K. A. Zoldak, and J. M. Forbes (2009), Solar cycle variability of Mars dayside exospheric temperatures: Model evaluation of underlying thermal balances, *Geophys. Res. Lett.*, *36*, L05201, doi:10.1029/2008GL036376.

Bougher, S. W., D. J. Pawlowski, and J. Murphy (2011a), Towards and understanding of the time dependent responses of the Martian upper atmosphere to dust events, Abstract P23E-08 presented at 2011 Fall Meeting, AGU, Washington, D. C.

Bougher, S. W., A. Ridley, D. Pawlowski, J. M. Bell, and S. Nelli (2011b), Development and validation of the ground-to-exosphere Mars GITM code: Solar cycle and seasonal variations of the upper atmosphere, in *Mars Atmosphere: Modelling and Observation*, edited by F. Forget, and E. Millour, pp. 379–381.

Bougher, S. W., D. J. Pawlowski, and J. R. Murphy (2014), Time dependent responses of the Martian upper atmosphere to the 2001 global dust storm using Mars GITM simulations, in *AAS/Division for Planetary Sciences Meeting Abstracts*, vol. 46, Am. Astron. Soc., Washington, D. C.

Bougher, S. W., D. A. Brain, J. L. Fox, F. González-Galindo, C. Simon-Wedlund, and P. G. Withers (2014a), Upper atmosphere and ionosphere, in *Mars II*, edited by B. Haberle et al., Cambridge Univ. Press, Cambridge, U. K.

Bougher, S. W., T. E. Cravens, J. Grebowksy, and J. Luhmann (2014b), The aeronomy of Mars: Characterization by MAVEN of the upper atmosphere reservoir that regulates volatile escape, *Space Sci. Rev.*, doi:10.1007/s11214-014-0053-7.

Chamberlin, P. C., T. N. Woods, and F. G. Eparvier (2008), Flare Irradiance Spectral Model (FISM): Daily component algorithms and results, *Space Weather*, *6*, S05001, doi:10.1029/2007SW000372.

Chassefière, E., and F. Leblanc (2004), Mars atmospheric escape and evolution; interaction with the solar wind, *Planet. Space Sci.*, *52*, 1039–1058, doi:10.1016/j.pss.2004.07.002.

Chaufray, J.-Y., F. Gonzalez-Galindo, F. Forget, M. Lopez-Valverde, F. Leblanc, R. Modolo, S. Hess, M. Yagi, P.-L. Blelly, and O. Witasse (2014), Three-dimensional Martian ionosphere model: II. Effect of transport processes due to pressure gradients, *J. Geophys. Res. Planets*, *119*, 1614–1636, doi:10.1002/2013JE004551.

Colegrove, F., F. Johnson, and W. Hanson (1966), Atmospheric composition in the lower thermosphere, *J. Geophys. Res.*, *71*, 2227–2236.

Conrath, B. J. (1975), Thermal structure of the Martian atmosphere during the dissipation of the dust storm of 1971, *Icarus*, *24*(1), 36–46.

Deng, Y., A. J. Ridley, and W. Wang (2008), Effect of the altitudinal variation of the gravitational acceleration on the thermosphere simulation, *J. Geophys. Res.*, *113*, A09302, doi:10.1029/2008JA013081.

Dowling, T., A. Fischer, P. Gierasch, J. Harrington, R. LeBeau, and C. Santori (1998), The Explicit Planetary Isentropic-Coordinate (EPIC) atmospheric model, *Icarus*, *132*(2), 221–238.

Fang, X., S. W. Bougher, R. E. Johnson, M. W. Ma, and Y. Liemohn (2013), The importance of pickup oxygen ion precipitation to the Mars upper atmosphere under extreme solar wind conditions, *Geophys. Res. Lett.*, *40*, 1922–1927, doi:10.1002/grl.50415.

Forbes, J. M., X. Zhang, E. R. Talaat, and W. Ward (2003), Nonmigrating diurnal tides in the thermosphere, *J. Geophys. Res.*, *108*(A1), 1033, doi:10.1029/2002JA009262.

Forbes, J. M., F. G. Lemoine, S. L. Bruinsma, M. D. Smith, and X. Zhang (2008), Solar flux variability of Mars' exosphere densities and temperatures, *Geophys. Res. Lett.*, *35*, L01201, doi:10.1029/2007GL031904.

Forget, F., F. Hourdin, R. Fournier, C. Hourdin, O. Talagrand, M. Collins, S. R. Lewis, P. L. Read, and J.-P. Huot (1999), Improved general circulation models of the Martian atmosphere from the surface to above 80 km, *J. Geophys. Res.*, *104*, 24,155–24,176, doi:10.1029/1999JE001025.

Forget, F., F. Montmessin, J.-L. Bertaux, F. González-Galindo, S. Lebonnois, E. Quemerais, A. Reberac, E. Dimarellis, and M. A. Lopez-Valverde (2009), Density and temperatures of the upper Martian atmosphere measured by stellar occultations with Mars Express SPICAM, *J. Geophys. Res.*, *114*, E01004, doi:10.1029/2008JE003086.

Fox, J. L. (2004), Response of the Martian thermosphere/ionosphere to enhanced fluxes of solar soft X-rays, *J. Geophys. Res.*, *109*, A11310, doi:10.1029/2004JA010380.

Fox, J. L., and K. Y. Sung (2001), Solar activity variations of the Venus thermosphere/ionosphere, *J. Geophys. Res.*, *106*, 21,305–21,336, doi:10.1029/2001JA000069.

Fox, J. L., and K. E. Yeager (2009), MGS electron density profiles: Analysis of the peak magnitudes, *Icarus*, *200*, 468–479, doi:10.1016/j.icarus.2008.12.002.

Fox, J. L., J. F. Brannon, and H. S. Porter (1993), Upper limits to the nightside ionosphere of Mars, *Geophys. Res. Lett.*, *20*, 1339–1342, doi:10.1029/93GL01349.

Fox, J. L., P. Zhou, and S. W. Bougher (1996), The Martian thermosphere/ionosphere at high and low solar activities, *Adv. Space Res.*, *17*, 203–218, doi:10.1016/0273-1177(95)00751-Y.

Fritts, D. C., L. Wang, and R. H. Tolson (2006), Mean and gravity wave structures and variability in the Mars upper atmosphere inferred from Mars Global Surveyor and Mars Odyssey aerobraking densities, *J. Geophys. Res.*, *111*, A12304, doi:10.1029/2006JA011897.

González-Galindo, F., M. López-Valverde, M. Angelats i Coll, and F. Forget (2005), Extension of a Martian general circulation model to thermospheric altitudes: UV heating and photochemical models, *J. Geophys. Res.*, *110*, E09008, doi:10.1029/2004JE002312.

González-Galindo, F., G. Gilli, and M. A. López-Valverde (2008), Nitrogen and ionospheric chemistry in the thermospheric LMD-MGCM, in *Third International Workshop on The Mars Atmosphere: Modeling and Observations*, pp. 9007, IPI Contribution 1447.

González-Galindo, F., F. Forget, M. López-Valverde, M. Angelats i Coll, and E. Millour (2009a), A ground-to-exosphere Martian general circulation model: 1. Seasonal, diurnal, and solar cycle variation of thermospheric temperatures, *J. Geophys. Res.*, *114*, E04001, doi:10.1029/2008JE003246.

González-Galindo, F., F. Forget, M. A. López-Valverde, and M. Angelats i Coll (2009b), A ground-to-exosphere Martian general circulation model: 2. Atmosphere during solstice conditions—Thermospheric polar warming, *J. Geophys. Res.*, *114*, E08004, doi:10.1029/2008JE003277.

González-Galindo, F., S. W. Bougher, and M. E. A. López-Valverde (2010), Thermal and wind structure of the Martian thermosphere as given by two general circulation models, *Planet. Space Sci.*, *58*, 1832–1849, doi:10.1016/j.pss.2010.08.013.

González-Galindo, F., J.-Y. Chaufray, M. A. López-Valverde, G. Gilli, F. Forget, F. Leblanc, R. Modolo, S. Hess, and M. Yagi (2013), 3D Martian Ionosphere model: I. The photochemical ionosphere below 180 km, *J. Geophys. Res. Planets*, *118*, 2105–2123, doi:10.1002/jgre.20150.

Gurnett, D. A., et al. (2005), Radar soundings of the ionosphere of Mars, *Science*, *310*, 1929–1933, doi:10.1126/science.1121868.

Haberle, R. M., et al. (1999), General circulation model simulations of the Mars Pathfinder atmospheric structure investigation/meteorology data, *J. Geophys. Res.*, *104*, 8957–8974, doi:10.1029/1998JE900040.

Haberle, R. M., J. L. Hollingsworth, A. Colaprete, A. F. C. Bridger, C. P. McKay, J. R. Murphy, J. Schaeffer, and R. Freedman (2003), The NASA/AMES Mars general circulation model: Model improvements and comparison with observations, in *Published Conference Abstract, International Workshop: Mars Atmosphere Modelling and Observations*.

Haider, S. A., K. K. Mahajan, and E. Kallio (2011), Mars ionosphere: A review of experimental results and modeling studies, *Rev. Geophys.*, *49*, RG4001, doi:10.1029/2011RG000357.

Hanson, W. B., S. Sanatani, and D. R. Zuccaro (1977), The Martian ionosphere as observed by the Viking retarding potential analyzers, *J. Geophys. Res.*, *82*, 4351–4363, doi:10.1029/JS082i028p04351.

Huestis, D. L., S. W. Bougher, J. L. Fox, M. Galand, R. E. Johnson, J. I. Moses, and J. C. Pickering (2008), Cross sections and reaction rates for comparative planetary aeronomy, *Space Sci. Rev.*, *139*, 63–105, doi:10.1007/s11214-008-9383-7.

Huestis, D. L., T. G. Slanger, B. D. Sharpee, and J. L. Fox (2010), Chemical origins of the Mars ultraviolet dayglow, *Faraday Discuss.*, *147*, 307–322.

Kasahara, A. (1974), Various vertical coordinate systems used for numerical weather prediction, *Mon. Weather Rev.*, *102*(7), 509–522.

Kasting, J. F., J. B. Pollack, and D. Crisp (1984), Effects of high CO2 levels on surface temperature and atmospheric oxidation state of the early Earth, *J. Atmos. Chem.*, *1*(4), 403–428.

Keating, G. M., et al. (1998), The structure of the upper atmosphere of Mars: In situ accelerometer measurements from Mars global surveyor, *Science*, *279*, 1672–1676, doi:10.1126/science.279.5357.1672.

Keating, G. M., M. E. Theriot, R. H. Tolson, S. W. Bougher, F. Forget, M. A. i Coll, and J. M. Forbes (2003), Recent detection of winter polar warming in the Mars upper atmosphere, *The Third International Mars Polar Science Conference,* p. 8033, Pasadena, Calif.

Keating, G. M., S. W. Bougher, M. E. Theriot, and R. H. Tolson (2008), Properties of the Mars upper atmosphere derived from accelerometer measurements, *Proceedings of the 37th COSPAR Scientific Assembly,* Montreal, Canada.

Kleinböhl, A., et al. (2009), Mars Climate Sounder limb profile retrieval of atmospheric temperature, pressure, and dust and water ice opacity, *J. Geophys. Res.*, *114*, E10006, doi:10.1029/2009JE003358.

Kleinböhl, A., J. T. Schofield, W. A. Abdou, P. G. J. Irwin, and R. J. de Kok (2011), A single scattering approximation for infrared radiative transfer in limb geometry in the Martian atmosphere, *J. Quant. Spectrosc. Radiat. Transfer*, *112*, 1568–1580, doi:10.1016/j.jqsrt.2011.03.006.

Krasnopolsky, V. A. (2010), Solar activity variations of thermospheric temperatures on Mars and a problem of CO in the lower atmosphere, *Icarus*, *207*, 638–647.

Leblanc, F., O. Witasse, J. Winningham, D. Brain, J. Lilensten, P.-L. Blelly, R. Frahm, J. Halekas, and J.-L. Bertaux (2006), Origins of the Martian aurora observed by spectroscopy for investigation of characteristics of the atmosphere of Mars (SPICAM) on board Mars Express, *J. Geophys. Res.*, *111*, A09313, doi:10.1029/2006JA011763.

Lefèvre, F., S. Lebonnois, F. Montmessin, and F. Forget (2004), Three-dimensional modeling of ozone on Mars, *J. Geophys. Res.*, *109*, E07004, doi:10.1029/2004JE002268.

Lillis, R. J., S. W. Bougher, F. González-Galindo, F. Forget, M. D. Smith, and P. C. Chamberlin (2010), Four Martian years of nightside upper thermospheric mass densities derived from electron reflectometry: Method extension and comparison with GCM simulations, *J. Geophys. Res.*, *115*, E07014, doi:10.1029/2009JE003529.

Liu, H.-L., et al. (2010), Thermosphere extension of the Whole Atmosphere Community Climate Model, *J. Geophys. Res.*, *115*, A12302, doi:10.1029/2010JA015586.

Lopez-Valverde, M., and M. Lopez-Puertas (2001), CO2 non-LTE cooling rate at 15 um and its parametrisation for the Mars atmosphere, *Esa contract: Martian environment Models, Instituto de Astrofisica de Andalucia*, Granada, Spain.

López-Valverde, M. A., D. P. Edwards, M. López-Puertas, and C. Roldán (1998), Non-local thermodynamic equilibrium in general circulation models of the Martian atmosphere: 1. Effects of the local thermodynamic equilibrium approximation on thermal cooling and solar heating, *J. Geophys. Res.*, *103*, 16,799–16,811, doi:10.1029/98JE01601.

López-Valverde, M. A., F. González-Galindo, and F. Foorget (2006), 1-D and 3-D modeling of the upper atmosphere of Mars, *2nd Workshop on Mars Atmosphere Modeling and Observations,* Granada, Spain.

Marsh, D. R., M. J. Mills, D. E. Kinnison, J.-F. Lamarque, N. Calvo, and L. M. Polvani (2013), Climate change from 1850 to 2005 simulated in CESM1 (WACCM), *J. Clim.*, *26*, 7372–7391.

Mason, E., and T. Marrero (1970), The diffusion of atoms and molecules, *Adv. At. Mol. Phy.*, *6*, 155–232.

Massman, W. (1998), A review of the molecular diffusivities of H2O, CO2, CH4, CO, O3, SO2, NH3, N2O, NO, and NO2 in air, O2 and N2 near STP, *Atmos. Environ.*, *32*(6), 1111–1127.

McCleese, D. J. E. A. (2008), Intense polar temperature inversion in the middle atmosphere of Mars, *Nat. Geosci.*, *1*, 745–749, doi:10.1038/ngeo332.

McDunn, T., S. Bougher, J. Murphy, A. Kleinböhl, F. Forget, and M. Smith (2013), Characterization of middle-atmosphere polar warming at Mars, *J. Geophys. Res. Planets*, *118*, 161–178, doi:10.1002/jgre.20016.

McDunn, T. L., S. W. Bougher, J. Murphy, M. D. Smith, F. Forget, J.-L. Bertaux, and F. Montmessin (2010), Simulating the density and thermal structure of the middle atmosphere (80–130 km) of Mars using the MGCM-MTGCM: A comparison with MEX/SPICAM observations, *Icarus*, *206*, 5–17, doi:10.1016/j.icarus.2009.06.034.

Medvedev, A., and E. Yiğit (2012), Thermal effects of internal gravity waves in the Martian upper atmosphere, *Geophys. Res. Lett.*, *39*, L05201, doi:10.1029/2012GL050852.

Medvedev, A., E. Yiğit, P. Hartough, and E. Becker (2011), Influence of gravity waves on the Martian atmosphere: General circulation modeling, *J. Geophys. Res.*, *116*, E10004, doi:10.1029/2011JE003848.

Medvedev, A., E. Yiğit, T. Kuroda, and P. Hartough (2013), General circulation modeling of the Martian upper atmosphere during global dust storms, *J. Geophys. Res. Planets*, *118*, 2234–2246, doi:10.1002/2013JE004429.

Medvedev, A., E. Yiğit, T. Kuroda, and P. Hartogh (2014), Response of the Martian upper atmosphere to lower atmospheric dust storms: GCM study, in *The Fifth International Workshop on the Mars Atmosphere: Modelling and Observation*, edited by F. Forget and M. Millour. id. 3201, vol. 1, p. 3201, Oxford, U. K., 13–16 Jan.

Mendillo, M., A. Marusiak, P.-G. Withers, D. Morgan, and D. Gurnett (2013), A new semi-empirical model of the peak electron density of the Martian ionosphere, *Geophys. Res. Lett.*, *40*, 5361–5365, doi:10.1002/2013GL057631.

MEPAG Goals Committee (2010), Mars Exploration Program Analysis Group (MEPAG) science goals.

Mischna, M. A., C. Lee, and M. Richardson (2012), Development of a fast, accurate radiative transfer model for the Martian atmosphere, past and present, *J. Geophys. Res.*, *117*, E10009, doi:10.1029/2012JE004110.

Montmessin, F., F. Forget, P. Rannou, M. Cabane, and R. Haberle (2004), Origin and role of water ice clouds in the Martian water cycle as inferred from a general circulation model, *J. Geophys. Res.*, *109*, E10004, doi:10.1029/2004JE002284.

Morgan, D., D. Gurnett, D. Kirchner, J. L. Fox, E. Nielsen, and J. Plaut (2008), Variation of the Martian ionospheric electron density from Mars Express radar soundings, *J. Geophys. Res.*, *113*, A09303, doi:10.1029/2008JA013313.

Moudden, Y., and J. Forbes (2008), Topographic connections with density waves in Mars' aerobraking regime, *J. Geophys. Res.*, *113*, E11009, doi:10.1029/2008JE003107.

Moudden, Y., and J. Forbes (2010), A new interpretation of Mars aerobraking variability: Planetary wave-tide interactions, *J. Geophys. Res.*, *115*, E09005, doi:10.1029/2009JE003542.

Mueller-Wodarg, I. C. F., R. V. Yelle, and M. E. A. Mendillo (2000), The thermosphere of Titan simulated by a global three-dimensional time-dependent model, *J. Geophys. Res.*, *105*, 20,833–20,856, doi:10.1029/2000JA000053.

Nier, A., and M. B. McElroy (1977), Composition and structure of Mars' upper atmosphere: Results from the neutral mass spectrometers on Viking 1 and 2, *J. Geophys. Res.*, *82*(28), 4341–4349.

Ockert-Bell, M. E., J. F. Bell III, J. B. Pollack, C. P. McKay, and F. Forget (1997), Absorption and scattering properties of the Martian dust in the solar wavelengths, *J. Geophys. Res.*, *102*(E4), 9039–9050.

Palmer, T., G. Shutts, and R. Swinbank (1986), Alleviation of a systematic westerly bias in general circulation and numerical weather prediction models through an orographic gravity wave drag parameterization, *Q. J. R. Meteorol. Soc.*, *112*, 1001–1039.

Pawlowski, D., and A. Ridley (2008), Modeling the thermospheric response to solar flares, *J. Geophys. Res.*, *113*, A10309, doi:10.1029/2008JA013182.

Pawlowski, D. J., and A. J. Ridley (2009a), Modeling the ionospheric response to the 28 October 2003 solar flare due to coupling with the thermosphere, *Radio Sci.*, *44*, RS0A23, doi:10.1029/2008RS004081.

Pawlowski, D. J., and A. J. Ridley (2009b), Quantifying the effect of thermospheric parameterization in a global model, *J. Atmos. Sol. Terr. Phys.*, *71*, 2017–2026, doi:10.1016/j.jastp.2009.09.007.

Pawlowski, D., S. Bougher, and A. Ridley (2010), The effect of solar variability on the Martian thermosphere and ionosphere system, in *38th COSPAR Scientific Assembly*, vol. 38, pp. 1100, Copernicus Meetings, Gottingen, Germany.

Pawlowski, D. J., S. W. Bougher, and P. Chamberlin (2011), Modeling the response of the Martian upper atmosphere to solar flares, Abstract P21A-1643 presented at 2011 Fall Meeting, AGU, Washington, D. C.

Pawlowski, D. J., S. W. Bougher, A. J. Ridley, and J. Murphy (2012), Modeling the Martian upper atmosphere using the Mars Global Ionosphere-Thermosphere Model (Invited)", in *Fall AGU*.

Pollack, J. B., O. B. Toon, and R. Boese (1980), Greenhouse models of Venus' high surface temperature, as constrained by Pioneer Venus measurements, *J. Geophys. Res.*, *85*(A13), 8223–8231.

Ridley, A., Y. Deng, and G. Tòth (2006), The Global Ionosphere-Thermosphere Model, *J. Atmos. Sol. Terr. Phys.*, *68*, 839–864.

Roble, R., E. Ridley, and R. Dickinson (1987), On the global mean structure of the thermosphere, *J. Geophys. Res.*, *92*, 8745–8758.

Roble, R., E. Ridley, A. Richmond, and R. Dickinson (1988), A coupled thermosphere/ionosphere general circulation model, *Geophys. Res. Lett.*, *15*, 1325–1328.
Roble, R. G. (1995), Energetics of the mesosphere and thermosphere, *AGU Geophys. Monogr.*, *87*, 1–22.
Rodrigo, R., E. García-Álvarez, M. López-González, and J. López-Moreno (1990), A nonsteady one-dimensional theoretical model of Mars' neutral atmospheric composition between 30 and 200 km, *J. Geophys. Res.*, *95*(B9), 14,795–14,810.
Sadourny, R., and K. Laval (1984), January and July performance of the LMD general circulation model, in *New Perspectives in Climate Modeling*, edited by A. Berger, and C. Nicolis, pp. 173–197, Elsevier, Amsterdam.
Safaeinili, A., W. Kofman, J. Mouginot, Y. Gim, A. Herique, A. B. Ivanov, J. J. Plaut, and G. Picardi (2007), Estimation of the total electron content of the Martian ionosphere using radar sounder surface echoes, *Geophys. Res. Lett.*, *34*, L23204, doi:10.1029/2007GL032154.
Schunk, R., and A. Nagy (2009), *Ionospheres*, Cambridge Univ. Press, Cambridge, U. K.
Seiff, A., and D. B. Kirk (1977), Structure of the atmosphere of Mars in summer at mid-latitudes, *J. Geophys. Res.*, *82*(28), 4364–4378.
Smith, D. E., and M. T. Zuber (1996), The Shape of Mars and the topographic signature of the hemispheric dichotomy, in *Lunar and Planetary Institute Science Conference Abstracts, Lunar and Planetary Institute Science Conference Abstracts*, vol. 27, pp. 1221, Lunar Planet. Inst., Houston, Tex.
Smith, M. D. (2004), Interannual variability in TES atmospheric observations of Mars during 1999–2003, *Icarus*, *167*, 148–165, doi:10.1016/j.icarus.2003.09.010.
Smith, M. D. (2009), THEMIS observations of Mars aerosol optical depth from 2002–2008, *Icarus*, *202*, 444–452, doi:10.1016/j.icarus.2009.03.027.
Stewart, A. I. (1972), Mariner 6 and 7 ultraviolet spectrometer experiment: Implications for CO_2+, CO and O airglow, *J. Geophys. Res.*, *77*(1), 54–68.
Stewart, A. I., C. Barth, C. Hord, and A. Lane (1972), Mariner 9 ultraviolet spectrometer experiment: Structure of Mars' upper atmosphere, *Icarus*, *17*(2), 469–474.
Stewart, A. I. F. (1987), Revised time dependent model of the Martian atmosphere for use in orbit lifetime and sustenance studies, *LASP-JPL Internal Rep., NQ-802429*, Jet Propul. Lab., Pasadena, Calif.
Stiepen, A., J.-C. Gerard, S.-W. Bougher, and F. Montmessin (2014), Martian thermosphere scale height from SPICAM dayglow measurements, *European Planetary Science Conference Abstracts*, *9*, 416.
Tolson, R., G. Keating, G. Cancro, J. Parker, S. Noll, and B. Wilkerson (1999), Application of accelerometer data to Mars global surveyor aerobraking operations, *J. Spacecraft Rockets*, *36*(3), 323–329.
Tolson, R., A. Dwyer, J. Hanna, G. Keating, B. George, P. Escalera, and M. Werner (2005), Application of accelerometer data to Mars Odyssey aerobraking and atmospheric modeling, *J. Spacecraft Rockets*, *42*(3), 435–443.
Tolson, R., G. Keating, R. Zurek, S. Bougher, C. Justus, and D. Fritts (2007), Application of acclerometer data to atmospheric modeling during Mars aerobraking operations, *J. Spacecraft Rockets*, *44*(6), 1172–1179.
Tolson, R. H., et al. (2008), Atmospheric modeling using accelerometer data during Mars Reconnaissance Orbiter aerobraking operations, *J. Spacecraft Rockets*, *45*(3), 511–518.
Toon, O. B., C. McKay, T. Ackerman, and K. Santhanam (1989), Rapid calculation of radiative heating rates and photodissociation rates in inhomogeneous multiple scattering atmospheres, *J. Geophys. Res.*, *94*(D13), 16,287–16,301.
Tóth, G., et al. (2005), Space weather modeling framework: A new tool for the space science community, *J. Geophys. Res.*, *110*, A12226, doi:10.1029/2005JA011126.
Vasavada, A., et al. (2012), Assessment of environments for Mars science laboratory entry, descent, and surface operations, *Space Sci. Rev.*, *170*(1-4), 793–835, doi:10.1007/s11214-012-9911-3.
Venkateswara Rao, N., N. Balan, and A. K. Patra (2014), Solar rotation effects on the Martian ionosphere, *J. Geophys. Res. Space Physics*, *119*, 6612–6622, doi:10.1002/2014JA019894.
Wilson, R. J. (2002), Evidence for nonmigrating thermal tides in the Mars upper atmosphere from the Mars global surveyor accelerometer experiment, *Geophys. Res. Lett.*, *29*(7), 1120, doi:10.1029/2001GL013975.
Withers, P. (2009), A review of observed variability in the dayside ionosphere of Mars, *Adv. Space Res.*, *44*, 277–307, doi:10.1016/j.asr.2009.04.027.
Withers, P., S. W. Bougher, and G. M. Keating (2003), The effects of topographically-controlled thermal tides in the Martian upper atmosphere as seen by the MGS accelerometer, *Icarus*, *164*, 14–32, doi:10.1016/S0019-1035(03)00135-0.
Withers, P., M. Mendillo, and D. Hinson (2006), Space weather effects on the Mars ionosphere due to solar flares and meteors, in *European Planetary Science Congress 2006*, 190, Copernicus Meetings, Gottingen, Germany.
Withers, P., M. Matta, and M. Mendillo (2010), The unusual electrodynamics of the ionosphere of Mars, in *European Planetary Science Congress 2010*, 68, Copernicus Meetings, Gottingen, Germany.
Woods, T. N., and G. J. Rottman (2002), Solar ultraviolet variability over time periods of aeronomic interest, in *Atmospheres in the Solar System: Comparative Aeronomy, Geophys. Monogr. Ser.*, vol. 130, edited by M. Mendillo, A. Nagy, and J. H. Waite, pp. 221, AGU, Washington, D. C.
Woods, T. N., F. G. Eparvier, S. M. Bailey, P. C. Chamberlin, J. Lean, G. J. Rottman, S. C. Solomon, W. K. Tobiska, and D. L. Woodraska (2005), Solar EUV experiment (SEE): Mission overview and first results, *J. Geophys. Res.*, *110*, A01312, doi:10.1029/2004JA010765.
Woods, T. N., et al. (2010), Extreme Ultraviolet Variability Experiment (EVE) on the Solar Dynamics Observatory (SDO): Overview of science objectives, instrument design, data products, and model developments, *Sol. Phys.*, *275*, 115–143, doi:10.1007/s11207-009-9487-6.
Zhang, M., J. Luhmann, and A. Kliore (1990), An observational study of the nightside ionospheres of Mars and Venus with radio occultation methods, *J. Geophys. Res.*, *95*(A10), 17,095–17,102.